ADVANCED FUNCTIONAL MATERIALS
www.afm-journal.de

Check for updates

Gold-Assisted Exfoliation of Large-Area Monolayer Transition Metal Dichalcogenides: From Interface Properties to Device Applications

*Salvatore Ethan Panasci, Emanuela Schilirò, Fabrizio Roccaforte, and Filippo Giannazzo**

Semiconductor transition metal dichalcogenides (TMDs), such as MoS_2, are currently regarded as key-enabling materials for sub-1 nm channel transistors, beyond-complementary metal–oxide–semiconductor electronic and optoelectronic devices and sensors. Owing to this wide application potential, several *bottom-up* and *top-down* synthesis approaches for these materials have been explored so far. Despite the huge progresses in scalable deposition methods (such as chemical vapor deposition, metal–organic chemical vapor deposition), exfoliated layers from bulk crystals still represent the benchmark for record electronic properties of TMDs. Among exfoliation approaches, metal-assisted mechanical exfoliation emerges as the most effective method to separate large-area (mm^2 to cm^2) single-crystalline monolayer membranes of TMDs (and many other 2D materials) from the parent bulk crystals. This paper reviews the state-of-the-art in this field, from current understanding of MoS_2 exfoliation mechanisms on Au (considered as a model system), to the main device applications of as-exfoliated and transferred large-area MoS_2 membranes (including Au/MoS_2/Au memristors, MoS_2 photodetectors, and field-effect transistors). Perspectives of this method in the realization of arrays of 2D heterojunction devices, including Moirè superlattice devices, and open challenges for its widespread application are finally discussed.

1. Introduction

Starting with the first report on the electronic properties of graphene obtained by mechanical exfoliation from graphite in 2004,[1] the research on two-dimensional (2D) materials has grown continuously during last two decades. To date, hundreds of 2D materials have been investigated experimentally,[2] whereas a database of up to 6000 monolayer structures has been recently compiled by predictive computational studies.[3] Most of the stable 2D materials can be obtained by the exfoliation of the parent layered bulk crystals existing in nature. Furthermore, the 2D counterparts of bulk crystals with "non-layered" structure, such as some Xenes (silicene, germanene, stanene),[4] 2D group-III nitrides (2D-GaN, InN, AlN),[5–8] and oxides (2D-In_2O_3 and Ga_2O_3),[9,10] have been obtained by proper synthetic strategies, i.e., the deposition on specific substrates or the intercalation in the confined space between epitaxial graphene and SiC.

Among 2D materials, transition metal dichalcogenides (TMDs) have been the object of increasing interest for their excellent mechanical, electrical, thermal, and optical properties.[11–13] This class of layered materials presents the chemical formula MX_2, where X is a chalcogen atom (S, Se, Te) and M is a transition metal of the IV B (Ti, Zr, Hf), V B (V, Nb, Ta), VI B (Mo,W), VII B (Tc, Re), and X B (Pt, Pt) groups of the periodic table[14,15] (see **Figure** 1a). The atoms within the individual X-M-X triatomic layers are covalently bonded, whereas a weak van der Waals (vdW) interaction is present between the stacked layers (see, e.g., Figure 1b). This allows to easily exfoliate single or few layers from the starting bulk crystals, similarly to the graphene obtained from HOPG.[16]

To date, molybdenum disulfide (MoS_2) has been the most investigated member of the TMDs family, due to its abundance in nature and chemical stability. In particular, its most common polytype (2H-MoS_2) exhibits semiconducting properties, with an indirect bandgap of ≈1.2–1.3 eV in the case of multilayers or bulk crystals, which changes into a direct bandgap of ≈1.8–1.9 eV when the thickness is reduced to a monolayer. This sizable bandgap, combined with a carrier mobility up to 200 $cm^2 V^{-1} s^{-1}$,[17] make MoS_2 appealing for a wide range of applications, including electronics, optoelectronics, photovoltaics, photocatalysis, and sensing.[18–23]

Due to these wide potentialities, many efforts have been carried out during the last years in the development of scalable methods to produce MoS_2 with high crystal quality and large area for future industrial applications. The synthesis approaches of MoS_2 and other TMDs explored so far can be grouped in two categories:

S. E. Panasci, E. Schilirò, F. Roccaforte, F. Giannazzo
Consiglio Nazionale delle Ricerche – Istituto per la Microelettronica e Microsistemi (CNR-IMM)
Strada VIII n.5, Catania 95121, Italy
E-mail: filippo.giannazzo@imm.cnr.it

The ORCID identification number(s) for the author(s) of this article can be found under https://doi.org/10.1002/adfm.202414532

© 2024 The Author(s). Advanced Functional Materials published by Wiley-VCH GmbH. This is an open access article under the terms of the Creative Commons Attribution License, which permits use, distribution and reproduction in any medium, provided the original work is properly cited.

DOI: 10.1002/adfm.202414532

© 2024 The Author(s). Advanced Functional Materials published by Wiley-VCH GmbH

ADVANCED FUNCTIONAL MATERIALS
www.afm-journal.de

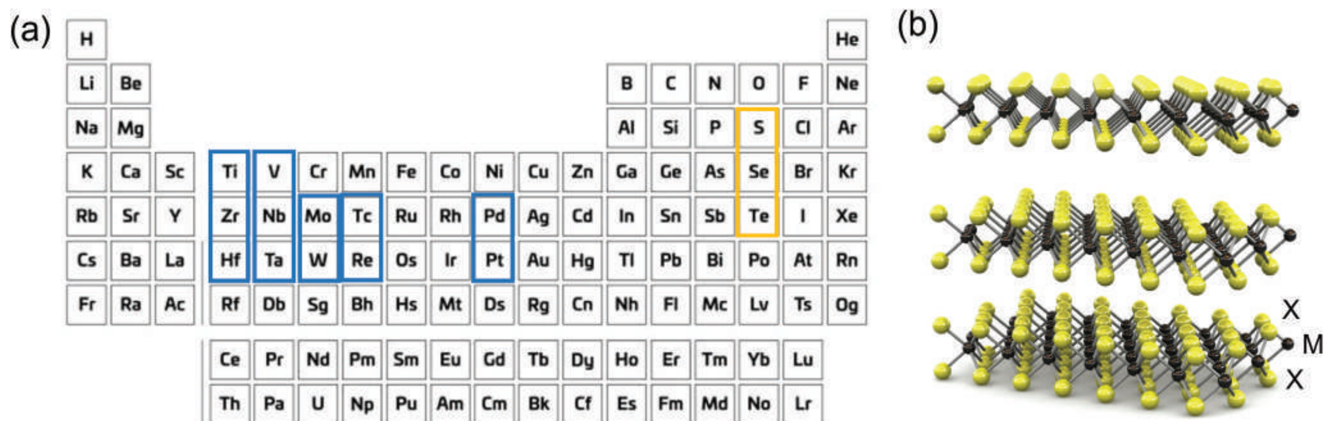

Figure 1. a) Periodic table of elements, with the indication of the chalcogen atoms (S, Se, Te) and transition metals of the groups *IV B* (Ti, Zr, Hf), *V B* (V, Nb, Ta), *VI B* (Mo,W), *VII B* (Tc, Re), and *X B* (Pt, Pt), from which TMDs are composed. b) Schematic illustration of the structure of a layered TMD, where X is a chalcogen atom and M is a transition metal. (b) Adapted with permission.[17] Copyright 2011, Springer Nature.

top-down approaches (based on the exfoliation of single or few layers from the corresponding bulk crystals by exploiting the weak interlayer bonding) and *bottom-up* approaches (including a number of chemical or physical deposition methods). As discussed more in detail in the next section, these different methods exhibit advantages and disadvantages, related to: i) the uniformity of the produced MoS_2 films (in terms of thickness, coverage, and crystalline domains size); ii) the required deposition/synthesis temperature; and iii) the possibility of directly growing or, alternatively, the need of transferring MoS_2 onto the target substrate for device applications.

When looking to the crystalline and electronic quality, MoS_2 flakes obtained by mechanical exfoliation still represent the benchmark for all the synthesis approaches. However, the reduced lateral size of these flakes and the low monolayer exfoliation yield make this approach suitable only for demonstration of small proof-of-concept devices. During last years, alternative mechanical exfoliation approaches based on the interaction between 2D materials and different metal surfaces (*metal-assisted mechanical exfoliation*) have been explored.[24] These approaches retain the advantages of traditional "scotch tape" mechanical exfoliation in terms of structural and electronic quality of produced 2D layers, while overcoming its main limitations (small lateral size of the flakes and poor thickness control). In particular, the "gold-assisted" mechanical exfoliation proved to be very effective in the case of MoS_2 and other TMDs, taking benefit of the strong interaction between Au and S atoms. Currently, it represents the best trade-off among top-down approaches to achieve high crystal quality, monolayer selectivity, and large area (from mm^2 to cm^2) of the exfoliated flakes. Due to these interesting features, this topic has been the object of several original papers and a number of recent review articles,[25,26] which have been mostly focused on the study of TMDs/Au interface properties and the exfoliation mechanisms.

This review article is aimed to provide the readers a comprehensive overview of recent developments of metal-assisted exfoliation of 2D materials, with a specific focus on Au-assisted exfoliation of MoS_2. The main approaches used to transfer MoS_2 membranes obtained by this method onto insulating or semiconducting substrates for device applications will be discussed, and some examples of devices will be presented. Furthermore, current limitations and open challenges to further exploit this approach will be discussed.

2. Bottom-Up and Top-Down Methods for Scalable Production of TMDs

A summary of the state-of-the-art bottom-up and top-down approaches for TMDs production is illustrated in **Figure 2**.

Bottom-up approaches are commonly regarded as the most suitable ones for perspective integration of MoS_2 in microelectronics production lines. During the last decade, chemical vapor deposition (CVD) methods using different kinds of precursors and growth conditions have been intensively explored to achieve large-area MoS_2 on different kinds of substrates.[27,35–37] The typically employed CVD apparatus used in academic laboratories consists of a tube furnace hosting crucibles with S and MoO_3 powders, whose vapors are transported to the heated sample surface by an inert carrier gas. Crystalline MoS_2 domains with sizes ranging from ≈1 to ≈100 µm have been obtained by this approach on different kind of substrates (amorphous, crystalline) at process temperatures ranging from 700 to 900 °C.[38,39] However, achieving uniform coverage and thickness control on wafer scale by this method remains a challenge, due to the difficulty of controlling the fluxes of the two vapor precursors from solid sources and the temperature uniformity on the sample. To circumvent these issues, two-step CVD processes have also been employed, consisting in the predeposition of Mo-based thin films on the sample's surface, followed by annealing in sulfur ambient to promote MoS_2 formation. As an example, uniform Mo or Mo-oxide (MoO_x) films with nanometer thickness can be predeposited by evaporation or sputtering,[40,41] pulsed laser deposition (PLD)[42] or atomic layer deposition (ALD),[43] and homogeneous MoS_2 films are obtained after high temperature (600–900 °C) sulfurization with the number of layers controlled by the initial Mo (MoO_x) thickness.[44–48] An alternative two-step approach consists in the dip-coating, drop-casting, or spin-coating of the sample's surface with a solution containing Mo precursors, such as the ammonium thiomolybdate $(NH_4)_2MoS_4$ or the ammonium molybdate tetrahydrate $(NH_4)_6Mo_7O_{24}$,[49] followed by annealing in sulfur

© 2024 The Author(s). Advanced Functional Materials published by Wiley-VCH GmbH

16163028, 0, Downloaded from https://onlinelibrary.wiley.com/doi/10.1002/adfm.202414532 by CNR Bologna, Wiley Online Library on [25/11/2024]. See the Terms and Conditions (https://onlinelibrary.wiley.com/terms-and-conditions) on Wiley Online Library for rules of use; OA articles are governed by the applicable Creative Commons License

16163028, 0, Downloaded from https://onlinelibrary.wiley.com/doi/10.1002/adfm.202414532 by CNR Bologna, Wiley Online Library on [25/11/2024]. See the Terms and Conditions (https://onlinelibrary.wiley.com/terms-and-conditions) on Wiley Online Library for rules of use; OA articles are governed by the applicable Creative Commons License

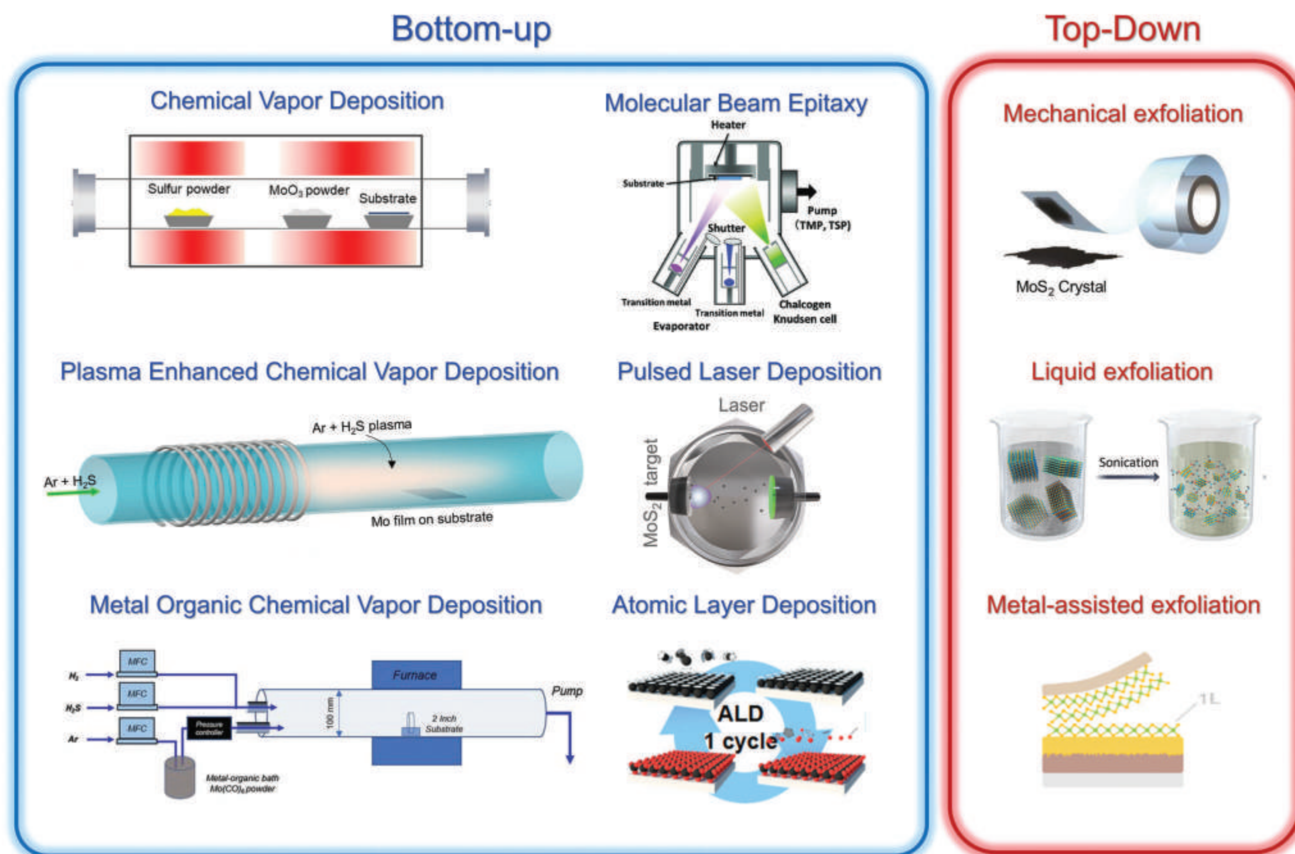

Figure 2. Schematic illustration of the state-of-the-art *bottom-up* and *top-down* approaches for TMDs production. CVD scheme adapted with permission.[27] Copyright 2020, American Chemical Society. PECVD scheme adapted with permission.[28] Copyright 2023, American Chemical Society. MOCVD scheme adapted with permission.[29] Copyright 2019, Elsevier. MBE scheme reproduced with permission.[30] Copyright 2019, J-STAGE. ALD scheme adapted with permission.[31]Copyright 2013, American Chemical Society. Mechanical exfoliation scheme adapted with permission.[32] Copyright 2012, IOP. Liquid Exfoliation scheme adapted with permission.[33] Copyright 2019, Springer Nature. Metal-assisted exfoliation scheme adpted with permission.[34] Copyright 2020, Wiley.

ambient. Although uniform MoS_2 films or large size crystalline MoS_2 domains have been obtained by this liquid precursors CVD approach, the mechanisms of MoS_2 formation and the role of residual contaminants need to be further understood. The relatively high temperatures employed in the above discussed CVD approaches can be a critical limitation for direct growth of TMDs on some kind of substrates, such as plastic substrates used for flexible devices applications, due to the low glass transition temperature of most of plastic materials.[50] For this reason, plasma enhanced chemical vapor deposition (PECVD) of MoS_2 has been recently developed as a low-temperature solution (150–400 °C) to overcome these limitations, enabling also a higher control in terms of thickness and nanostructure uniformity formation due to the presence of active species in the plasma.[28,50,51] Bala et al.[28] demonstrated the fabrication of flexible MoS_2-based memristors with excellent resistive switching performances and endurances (>350 cycles), achieved by direct growth on polyimide at 250 °C. The recent application of metal–organic chemical vapor deposition (MOCVD) represented a key advancement toward wafer scale growth of MoS_2 and other TMDs,[29,52,53] since the use of suitable metal organic gas precursors (e.g., $Mo(CO)_6$ and $(C_2H_5)_2S$ as the molybdenum and sulfur precursors) allows a superior control of the deposition process. Furthermore, the deposition of crystalline MoS_2 at low temperatures (<400 °C), compatible with the back-end-of-line (BEOL) integration on silicon complementary metal–oxide–semiconductor (CMOS) circuits, has been recently demonstrated by Zhu et al.[54] using a customized MOCVD process. The wafer scale deposition of ultrathin MoS_2 films at low temperatures (from 350 °C down to 60 °C) has also been recently investigated by the ALD technique using suitable precursors.[31,55–57] However, the deposited films are typically amorphous/nanocrystalline, and a postdeposition annealing step in sulfur ambient at temperatures of 900–1000 °C is typically required to obtain crystalline MoS_2. Besides CVD approaches, also physical deposition methods have been employed in the last years for large-area MoS_2 growth. Among these, pulsed laser deposition (PLD) from a MoS_2 target resulted in the epitaxial growth of highly uniform MoS_2 films on hexagonal crystalline substrates (sapphire, 4H-SiC, GaN) at temperatures ≈700 °C.[58–60] Molecular beam epitaxy (MBE) has also been recently employed to obtain epitaxial MoS_2 growth on different substrates, including sapphire, group-III Nitrides, h-BN.[30,61,62]

Top-down approaches rely on the exfoliation of single or few layers 2D films from the corresponding bulk crystals, by

 © 2024 The Author(s). Advanced Functional Materials published by Wiley-VCH GmbH

16163028, 0, Downloaded from https://onlinelibrary.wiley.com/doi/10.1002/adfm.202414532 by CNR Bologna, Wiley Online Library on [25/11/2024]. See the Terms and Conditions (https://onlinelibrary.wiley.com/terms-and-conditions) on Wiley Online Library for rules of use; OA articles are governed by the applicable Creative Commons License

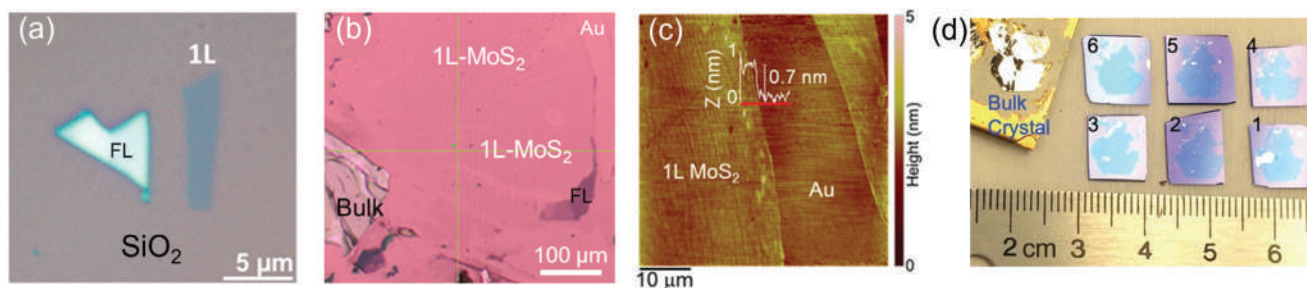

Figure 3. Optical images of MoS_2 flakes exfoliated on an a) SiO_2/Si substrate and b) Au film onto an SiO_2/Si substrate. c) AFM morphology and height line-scan (insert) of Au-exfoliated 1L MoS_2 membrane with a crack. d) Photo of a bulk MoS_2 stamp and a set of six Au/SiO_2 samples with MoS_2 membranes with the same shape and size exfoliated from the stamp. (a) Reproduced with permission.[86] Copyright 2014, American Chemical Society. (b) and (c) Reproduced with permission.[87] Copyright 2021, American Chemical Society. (d) Reproduced with permission.[88] Copyright 2020, AAAS.

exploiting the weak (vdW) interlayer bonding. As a matter of fact, the classical mechanical exfoliation (i.e., the "scotch-tape" method)[32] still provides the highest crystalline MoS_2 quality, despite the low monolayer yield and small lateral size of the obtained flakes. In particular, the typical lateral size of mechanically exfoliated flakes of MoS_2 (and other TMDs) is in the order of micrometers, a factor of ≈10 lower than the typical size of graphene flakes obtained from HOPG. This lower exfoliation yield of monolayer MoS_2 can be ascribed, in part, to the higher interlayers force constant per unit area (≈29×10^{18} N m^{-3}) in MoS_2 bulk crystals, as compared to that for HOPG (12.8×10^{18} N m^{-3}).[63,64]

To increase the exfoliation yield, liquid exfoliation methods[33] have been developed, which are low-cost and easy approaches, allowing to produce a large quantity of MoS_2 nanosheets by dispersion in solvents or ionic species.[65–67] Notably, the liquid intercalation of bulk MoS_2 by ionic species (such as lithium) is a very effective exfoliation approach, which is, however, typically accompanied by the conversion of the semiconductor 2H-phase (with octahedral coordination of Mo atoms) to the metallic 1T-phase (trigonal coordination).[68–71] Therefore, the MoS_2 films obtained by spin-coating or drop-casting of the liquid exfoliated solutions on a substrate must be typically subjected annealing treatments to partially restore the 2H- phase. Furthermore, since these films are composed by the overlap of large number of nanoflakes, they exhibit much higher resistivity and lower mobility as compared to MoS_2 films deposited by bottom-up methods. Hence, the liquid exfoliation approach is more promising for low-cost applications not requiring high carrier mobility, such as some flexible electronics applications,[72,73] catalysis,[74,75] and energy storage systems.[76–78]

In the framework of top-down methods, the metal-assisted exfoliation, and particularly the Au-assisted exfoliation represents the best trade-off to achieve high crystal quality, monolayer selectivity, and large area (from mm^2 to cm^2) of the exfoliated TMDs flakes.[34,79–85] **Figure** 3a,b shows the comparison between representative optical microscopy images of a) MoS_2 flakes with mm lateral sized and few-layers (FL) or 1L thickness exfoliated on an SiO_2/Si substrate,[86] and b) a large-area (several 100 mm) MoS_2 membrane exfoliated on an Au film deposited on SiO_2.[87] This membrane is mostly composed by 1L, with the presence of some FL and thicker (bulk) regions, as deduced by the optical contrast. The 1L thickness is also confirmed by the atomic force microscopy (AFM) image and height line profile in Figure 3c, collected in a region with a crack in the 1L MoS_2 membrane. An interesting aspect of MoS_2 exfoliation from a bulk MoS_2 stamp on the Au surface is the high repeatability of the process, as illustrated in Figure 3d, showing the bulk MoS_2 stamp and a set of six Au/SiO_2 samples with MoS_2 membranes with the same shape and size exfoliated from the stamp.

3. Metal-Assisted Mechanical Exfoliation of TMDs

3.1. Basic Mechanisms

This section reports an overview of the main models considered so far to explain the monolayer selective exfoliation of TMDs on Au and other metal surfaces.

A first model explains the effectiveness of TMDs exfoliation on Au surfaces in terms of the well-known strong interaction between sulfur and other chalcogen atoms with gold.[89,90] As an example the affinity between S and Au is commonly employed to obtain self-assembled monolayers of thiolate molecules on Au surfaces or the formation of gold–thiolate complexes,[89,91] with a bond strength of the adsorbed S atoms on Au as high as ≈40–50 kcal mol^{-1} (188.28 kJ mol^{-1}).[92] The exfoliation of MoS_2 and other TMDs on Au surface exploits this strong materials affinity, although the exact nature of the interaction involved in the exfoliation process is still matter of debate.

Several authors have proposed a "strong" van der Waals interaction as the main bonding mechanism between the TMDs and Au surface.[93–95] Thus, when an MoS_2 layered crystal is placed in contact with a gold substrate, the equilibrium distance between the center of the Mo—Au atomic planes (indicated in **Figure** 4a as d_{vdw} (Mo—Au)) is estimated in a range between 4.0 and 5.1 Å.[95] Such distance is smaller than the interlayer distance between the Mo—Mo planes d_{vdw} (Mo—Mo) ≈ 6.2 Å of the stacked MoS_2 layers,[96] consistently with the stronger MoS_2/Au interaction compared with the MoS_2 vdW interlayer bond. Figure 4b shows the binding energy (E_b) per unit cell of 1L MoS_2 on Au(111) as a function of the Mo—Au distance, obtained by first-principles atomistic calculations.[95] The blue dashed horizontal line represents the MoS_2–MoS_2 interlayers binding energy ($E_{b(MoS2\text{-}MoS2)} = -0.34$ eV) in the bulk MoS_2 crystal. According to this plot, the exfoliation of 1L MoS_2

© 2024 The Author(s). Advanced Functional Materials published by Wiley-VCH GmbH

16163028, 0, Downloaded from https://onlinelibrary.wiley.com/doi/10.1002/adfm.202414532 by CNR Bologna, Wiley Online Library on [25/11/2024]. See the Terms and Conditions (https://onlinelibrary.wiley.com/terms-and-conditions) on Wiley Online Library for rules of use; OA articles are governed by the applicable Creative Commons License

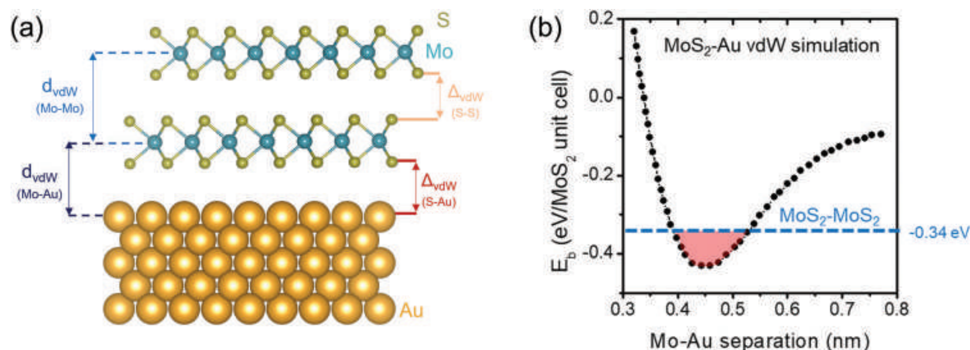

Figure 4. a) Schematic illustration of layered MoS_2 on an Au substrate where the distance between two atomic Mo—Mo planes (d_{vdw}(Mo—Mo)), the vdW gap between two atomic S—S planes (Δ_{vdW}(S—S)), the distance between Mo—Au (d_{vdw}(Mo—Au)), and the vdW gap between S—Au planes (Δ_{vdW}(S—Au)) are indicated. b) Binding energy (E_b) of 1L MoS_2 with Au as a function of Mo—Au separation. Reproduced with permission.[95] Copyright 2018, American Chemical Society.

from its bulk crystal on the Au surface is obtained when the Mo—Au separation is in the range between 4.0 and 5.1 Å, resulting in a $|E_b| > |E_{b(MoS2\text{-}MoS2)}|$ (red region of the curve below the blue-dashed line). In particular, the minimum of the E_b versus $d_{Mo\text{-}Au}$ curve ($E_b = -0.41$ eV) corresponds to the equilibrium separation $d = 4.5$ Å.[95]

Other authors indicated a covalent-like quasi-bonding (CLQB) as the most appropriate description of the interaction between MoS_2 and Au substrate.[97–99] CLQB is a noncovalent interaction with typical interaction energy of −0.5 eV per unit cell,[100–102] which is stronger than common vdW interactions and weaker compared to covalent bonds, where interlayer electronic hybridization occurs. This kind of interaction results from the balance between the long-range dispersion attraction induced by the high polarizability of some 2D materials and the short-range Pauli repulsion due to the wavefunction overlap.[99] A CLBQ with 2D materials typically occurs in the case of substrate materials with the Fermi level inside a partially filled band composed by s- or p- electrons and high polarizable electrons densities, the requirements of which are fully satisfied by noble metals.[99]

The stronger Au–MoS_2 interaction than the MoS_2 vdW interlayer bonding allows to explain the effective exfoliation of MoS_2 ultrathin films on gold surfaces. However, this first model does not completely account for the monolayer selective exfoliation, i.e., how cleaving preferentially occurs between the first MoS_2 layer (MoS_2(1)) in contact with Au and the second MoS_2 layer (MoS_2(2)). In fact, although cleaving preferentially occurs at interfaces with lower binding energy, the model does not account for a lower MoS_2(1)/MoS_2(2) interlayer binding energy than the bulk MoS_2 crystal.

A second model considered the role of strain in the MoS_2(1) associated to lattice mismatch with Au (or other metal surfaces) as the main origin of monolayer selectivity.[103,104] In fact, tensile strain results in a reduced atomic density of the MoS_2(1) layer and an increased interlayer distance, reducing the attractive vdW interactions between MoS_2(1) and MoS_2(2). Indeed, as shown in Section 3.3, monolayer MoS_2 exfoliated on Au may be subjected to significant tensile strain values (few %), depending on the Au/MoS_2 interface quality and preparation. However, this second model cannot explain monolayer-selective exfoliation of MoS_2 on other metal surfaces, such as Pd, with negligible lattice mismatch to MoS_2.[105]

More recently, Corletto et al.[106] proposed a third model, combining both lattice mismatch strain and the electrostatics (i.e., Schottky barrier formation and charge transfer) at MoS_2/metal interfaces, in order to provide a general description of monolayer-selective exfoliation yield on different metal surfaces. **Figure 5a** illustrates the energy band diagram of a metal/MoS_2 system before and after contact, showing the formation of a Schottky barrier at the interface with a built-in potential $\Phi_i = W_M - \chi_{MoS2} - (E_F - E_C)$, with W_M the metal work-function, χ_{MoS2} the electron affinity, and E_C the conduction band energy of MoS_2, and E_F the Fermi energy. Figure 5b shows the electron density variation (i.e., electron depletion) for MoS_2 in contact with different metals, with respect to isolated MoS_2. Hence, when bulk MoS_2 goes in contact with a metal surface, the built-in electric field E associated with the Schottky junction is responsible for an increased effective MoS_2(1)/MoS_2(2) interlayer distance and a weakening of the interlayer bond (as illustrated schematically in Figure 5c), whereas the electron depletion is responsible for a change in MoS_2 polarizability. According to this model, the MoS_2(1)/MoS_2(2) interlayer binding energy (E_{Int}) can be expressed as:

$$E_{Int} = E_{Int0} + \Delta E_{Int}(\varepsilon) + \Delta E_{Int}(E) + \Delta E_{Int}(n) \quad (1)$$

where E_{Int0} is the initial vdW interlayer bond before contact formation, whereas $\Delta E_{Int}(\varepsilon)$, ΔE_{Int} (E), and $\Delta E_{Int}(n)$ are the variations due to lattice mismatch strain, Schottky electric field, and electron depletion, respectively. The plot in Figure 5d shows a collection of experimental values of built-in potential (Φ_Δ) and strain (ε) for MoS_2/metal interfaces, extracted from different papers. Furthermore, the calculated MoS_2(1)/MoS_2(2) interface energies E_{int} are also reported, considering only strain effects (vertical dotted lines) and both strain and electrostatic effects (dashed lines). This graph confirms that monolayer MoS_2 exfoliation selectivity on different metal surfaces can be properly described only by the combination of these effects. On the other hand, this graph shows the large spread in the experimental values of strain ε and Φ_Δ, suggesting a strong dependence of these values on the preparation conditions of metal/MoS_2 interface.

© 2024 The Author(s). Advanced Functional Materials published by Wiley-VCH GmbH

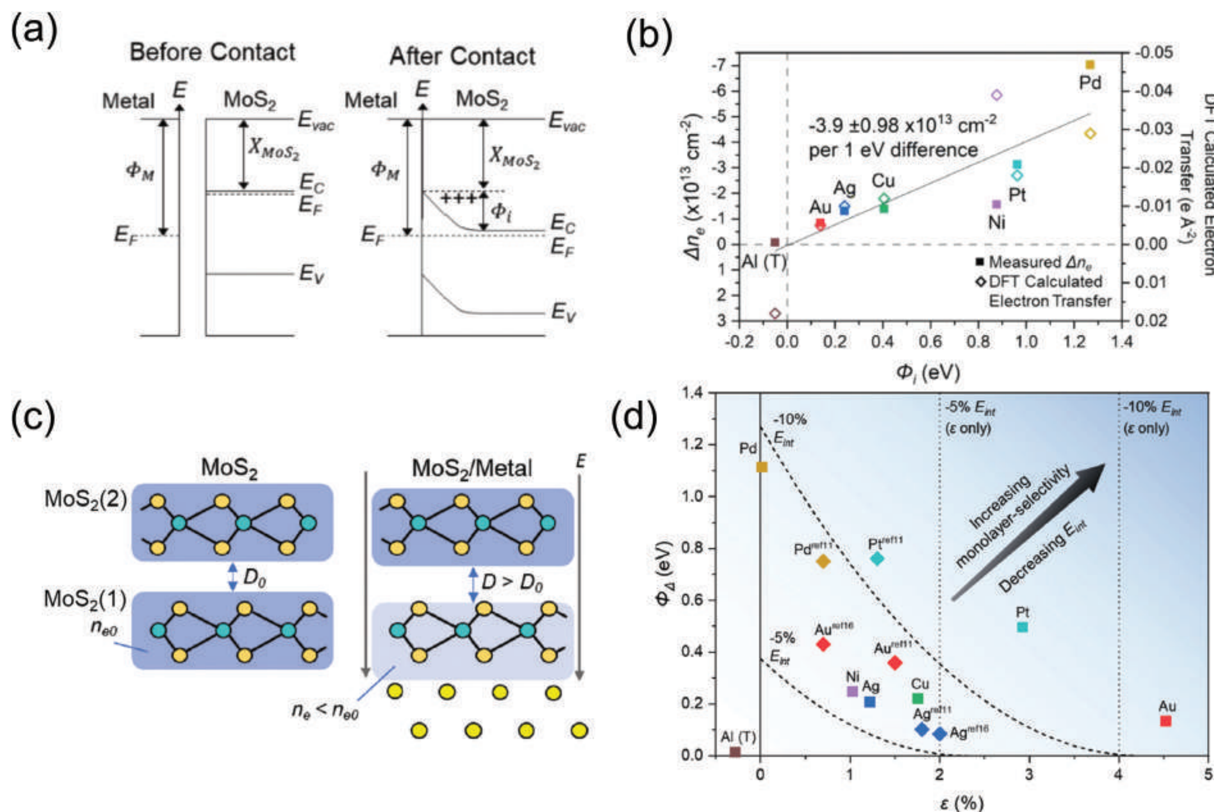

Figure 5. a) Schematic band diagram of a metal/MoS_2 system before and after Schottky contact formation, illustrating the built-in potential Φ_i and electrons depletion at MoS_2 surface. b) Electron density variation for 1L MoS_2 in contact with different metals (with respect to isolated 1L MoS_2), evaluated from Raman spectra (left column) or by DFT calculations (right column) versus the built-in potential Φ_i. c) Schematic illustration of the increase of the $MoS_2(1)/MoS_2(2)$ interlayer distance due to the built-in electric field and electron depletion after contact formation. d) Plot of experimental values of the built-in potential (Φ_Δ) and strain (ε) for MoS_2/metal interfaces, extracted from different papers, and calculated $MoS_2(1)/MoS_2(2)$ interface energies E_{int} considering only strain effects (vertical dotted lines) and both strain and electrostatic effects (dashed lines). Reproduced with permission.[106] Copyright 2024, American Chemical Society.

In the next section, the key experimental parameters playing a role in the exfoliation of monolayer MoS_2 on gold surfaces, considered as a model system, will be discussed.

3.2. Key Experimental Parameters for Monolayer MoS_2 Exfoliation on Au

From the experimental viewpoint, the morphology of the Au surface (i.e., its roughness) and its cleanness (i.e., the absence of adsorbates) are two key parameters affecting the 1L MoS_2 exfoliation yield. As reported by Velicky et al.,[95] a high roughness of the Au surface causes a reduction of the "effective" contact area with the bulk MoS_2 stamp, resulting in a lower 1L MoS_2 exfoliation yield. The impact of different roughness values on the local interaction between MoS_2 and Au is schematically illustrated in **Figure** 6a,b. Furthermore, the experimental results in Figure 6c demonstrate the drastic decrease of 1L MoS_2 exfoliation yield from ≈95% to ≈10% by increasing the Au surface roughness from ≈0.68 to ≈1.44 nm. Thus, the optimization of the physical vapor deposition (PVD) process of Au thin films, such as magnetron sputtering and electron-beam evaporation, is essential to achieve an improved MoS_2-Au surface contact.

The adsorption of organic contaminants (especially adventitious carbon) on as-prepared Au surface during prolonged exposure to air is another key factor influencing the strength and uniformity of MoS_2–Au interaction. In particular, it has been estimated that, in the case of a flat Au surface, exposure to air for ≈9–10 min results in the formation an inhomogeneous contaminant layer, whereas a complete coverage by such organic film is achieved for exposure times >15 min, as schematically illustrated in Figure 6d,f. As a matter of fact, the presence of this interlayer partially or completely screens the interaction between MoS_2 and Au. As a result, from the experimental viewpoint, a very efficient 1L MoS_2 exfoliation was achieved from few seconds up to ≈5 min from the gold deposition, whereas a significant decrease in the exfoliation yield of 1L (and a corresponding increase for multilayers) was observed after 8–10 min,[95] as shown in Figure 6g.

3.3. Morphological, Structural, Vibrational, and Optical Properties of Exfoliated MoS_2 on Gold

The morphological, vibrational, and light emission properties of exfoliated MoS_2 membranes on Au surfaces have been widely investigated by different research groups, using a variety of

© 2024 The Author(s). Advanced Functional Materials published by Wiley-VCH GmbH

16163028, 0, Downloaded from https://onlinelibrary.wiley.com/doi/10.1002/adfm.202414532 by CNR Bologna, Wiley Online Library on [25/11/2024]. See the Terms and Conditions (https://onlinelibrary.wiley.com/terms-and-conditions) on Wiley Online Library for rules of use; OA articles are governed by the applicable Creative Commons License

16163028, 0, Downloaded from https://onlinelibrary.wiley.com/doi/10.1002/adfm.202414532 by CNR Bologna, Wiley Online Library on [25/11/2024]. See the Terms and Conditions (https://onlinelibrary.wiley.com/terms-and-conditions) on Wiley Online Library for rules of use; OA articles are governed by the applicable Creative Commons License

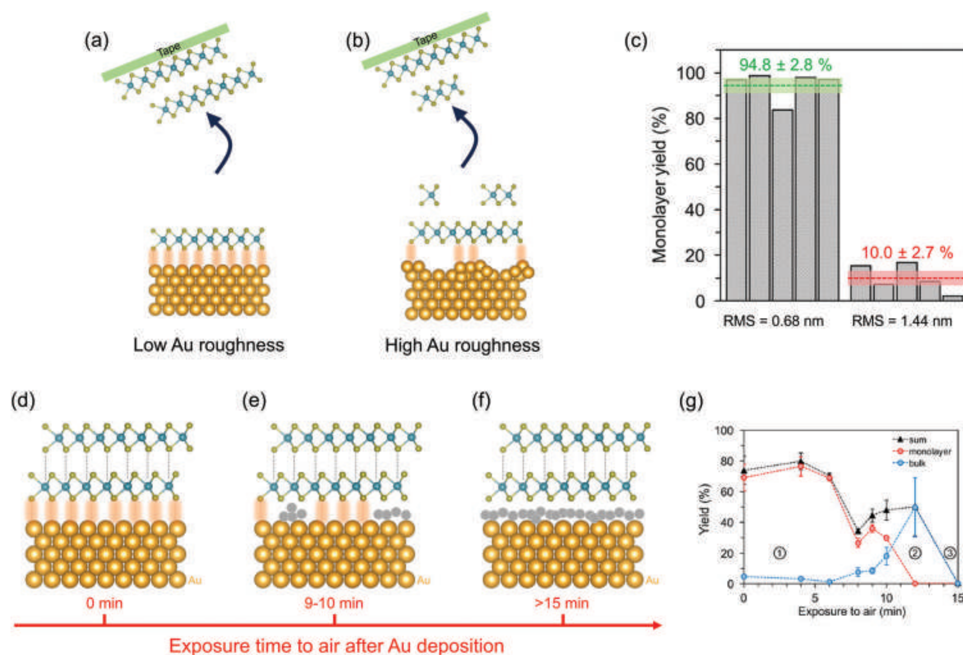

Figure 6. a,b) Schematic illustrations of 1L MoS_2 exfoliation on Au substrates with low and high roughness. c) Histograms of the 1L exfoliation yield for both the Au substrates. Schematic of the organic contaminations on the gold surface after d) 0–15 s, e) 9–10 min and f) >15 min of exposure to air. g) Corresponding graph of the exfoliation yield (%) as a function of the exposure time to air (min). All the figures are reproduced with permission.[95] Copyright 2018, American Chemical Society.

microscopic (AFM and transmission electron microscopy [TEM]) and spectroscopic techniques (micro-Raman and PL spectroscopies). In particular, micro-Raman spectroscopy is a powerful method, providing critical information on the crystal quality, thickness, strain, and doping effects induced by substrates on 2D materials.[107–110]

Raman analyses reported in the literature clearly show how the interaction with the substrate affects the main vibrational features of 1L or few-layer MoS_2 exfoliated on gold, due to substrate-induced strain and doping, and results in a quenching of PL emission. However, significant differences in the strain and doping of MoS_2 and in the PL intensity reduction are observed among different reports, indicating how several factors including the Au morphology and surface preparation influence the properties of MoS_2 films on the metal substrate.

In the following some examples showing this variability in the experimental results are illustrated.

Figure 7a shows the AFM morphology of 1L MoS_2 exfoliated on the surface of an Au film (15 nm thick), deposited by e-beam evaporation. This image illustrates how the 1L MoS_2 membrane adapts to the Au films topography. Figure 7b, continuous lines, shows a set of Raman spectra collected on MoS_2 with different thickness (1L, 2L, 3L, and bulk) exfoliated on the same Au surface. For comparison, the Raman spectra of 1L, 2L, 3L, and bulk MoS_2 on SiO_2 are also reported as dashed lines. While no significant substrate-related differences in the in-plane (E_{2g}) and out-of-plane (A_{1g}) Raman modes can be observed for bulk and 3L MoS_2 samples, slight differences in the E_{2g} width appear for 2L MoS_2 on Au with respect to SiO_2. On the other hand, very strong differences in the in-plane (E′) and out-of-plane (A'_1) vibrational features were found for 1L MoS_2 supported by the two substrates. In particular, for 1L MoS_2 on Au, the E′ mode was subjected to a strong redshift and broadening, while the A'_1 mode was split in two components, defined as A'_1(L) and A'_1(H). These peculiar features have been reported by different authors in literature,[111–116] although the interpretation of their origin is still matter of debate. As an example, Velicky et al.[111] explained the splitting of the A'_1 mode as a consequence of the roughness of the e-beam deposited Au film, which results in the co-existence (within the area probed by the laser spot) of nanoscale 1L MoS_2 regions in direct contact with Au and of suspended regions, as illustrated in Figure 7c. Since the A'_1 mode is known to be sensitive to the local doping of 1L MoS_2, the separation of the A'_1(L) and A'_1(H) components was associated to a difference in substrate-induced doping. Furthermore, the strong E′ redshift was connected to a high tensile strain (between 0.8% and 1.9%) of the 1L MoS_2 membrane in this configuration. Pollmann et al.[112] considered the intensity ratio between the two A'_1(L) and A'_1(H) components as a way to evaluate the degree of contact strength (or contact area) between 1L MoS_2 and Au. Noteworthy, such a scenario from Raman characterization (i.e., a large E′ redshift and A'_1 splitting) was typically accompanied by a strong quenching of the PL emission from 1L MoS_2 on Au.[111]

On the other hand, other authors reported a different scenario from micro-Raman and PL analyses of 1L MoS_2 exfoliated on Au films, i.e., the lack of splitting in the A'_1 and a small redshift of the E′ Raman peaks, accompanied by an evident (although significantly quenched) PL signal from MoS_2.[87,99,114,117] **Figure** 8a shows the AFM surface morphology of 1L MoS_2 exfoliated on a very flat Au films (deposited by DC sputtering on SiO_2 with a Ni adhesion layer). The comparison of surface roughness values of the bare and 1L MoS_2 covered Au areas (Figure 8b) clearly

 © 2024 The Author(s). Advanced Functional Materials published by Wiley-VCH GmbH

16163028, 0, Downloaded from https://onlinelibrary.wiley.com/doi/10.1002/adfm.202414532 by CNR Bologna, Wiley Online Library on [25/11/2024]. See the Terms and Conditions (https://onlinelibrary.wiley.com/terms-and-conditions) on Wiley Online Library for rules of use; OA articles are governed by the applicable Creative Commons License

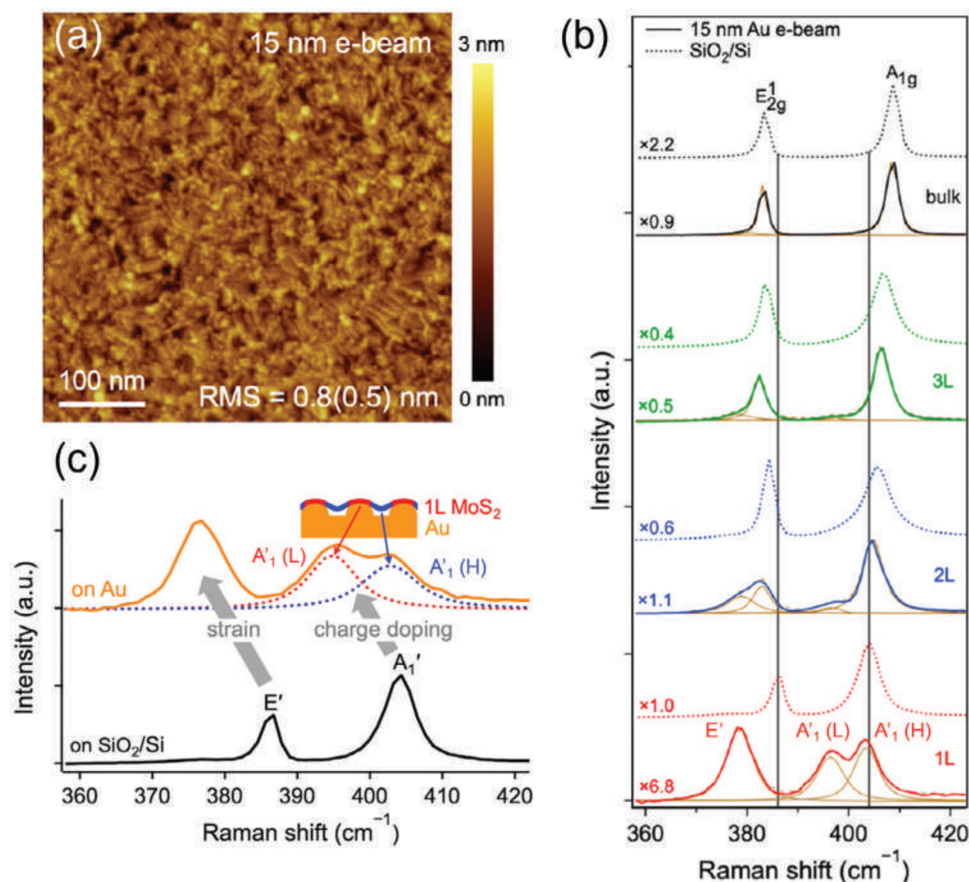

Figure 7. a) AFM morphology of 1L MoS_2 exfoliated on the surface of an Au film (15 nm thick, deposited by e-beam evaporation). b) Raman spectra of MoS_2 with different thickness in contact with the Au surface (continuous line) and on SiO_2 (dashed lines): bulk (black spectra), 3L MoS_2 (green spectra), 2L MoS_2 (blue spectra), and 1L MoS_2 (red spectra). c) Details of the Raman features for 1L MoS_2 on SiO_2 (black line) and on Au (orange line), with deconvolution analysis. All the figures are reproduced with permission.[111] Copyright 2020, American Chemical Society.

demonstrate how the MoS_2 membrane is perfectly conformal with the flat Au surface. The highly conformal vdW interface between 1L MoS_2 and Au, with a Mo—Au distance ($d_{\text{Mo-Au}}$) in the range between 4.0 and 4.4 Å, was evaluated by atomic resolution cross-sectional HAADF-STEM (Figure 8c).

Figure 8d shows a set of typical Raman spectra collected on MoS_2 membranes with different thickness (1L, 2L, few layers, and bulk) exfoliated on that Au surface (continuous line), and, for comparison, on MoS_2 membranes transferred onto an Al_2O_3/Si surface (dashed lines). The vertical gray lines indicate the E′ and A'_1 modes for 1L MoS_2 on the insulating Al_2O_3 substrate, with a peaks' separation $\Delta\omega \approx 18$ cm^{-1}, typically associated with monolayer thickness.[119] Noteworthy, the E′ peak for 1L MoS_2 on Au exhibits a small redshift with respect to 1L MoS_2 on Al_2O_3, which was associated with a small tensile strain (≈0.2%). With increasing the number of MoS_2 layers, the separation $\Delta\omega$ between the in-plane ($E_{2\ g}$) and out-of-plane ($A_{1\ g}$) Raman peaks increases (as commonly observed), and the individual peak positions become independent on the kind of substrate (Au or Al_2O_3).

Finally, Figure 8e,f shows the PL spectra collected on 1L, few layers and bulk MoS_2 films exfoliated on Au and transferred onto A_2O_3/Si. For all the spectra, the intensities have been normalized to the respective Raman peaks, to allow a comparison between different MoS_2 thicknesses and different substrates. Noteworthy, for Au-supported 1L MoS_2 PL emission is significantly quenched (although still measurable), and the PL peak exhibits a red-shift, as compared to the same 1L membrane exfoliated on Au and subsequently transferred onto Al_2O_3.[119]

The correlative plot of E′ and A'_1 Raman peak positions represents an effective approach to evaluate the strain (ε) and doping (n) of 1L MoS_2 membranes, as demonstrated by different authors.[87,120–123] In **Figure 9**, we used this kind of plot to provide an overview of recent literature results of Raman characterization on 1L MoS_2/Au systems. Here, the red (black) continuous lines are the strain (doping) lines, which represent the theoretical ($\omega_{E'}$; $\omega_{E'}$) relations for an ideally undoped (unstrained) 1L MoS_2. These two lines cross in a point (gray square) corresponding to the literature values of the E′ and A'_1 peaks' wavenumbers for a suspended 1L MoS_2 ($\omega^{o}_{E'} = 385$ cm^{-1}; $\omega^{o}_{A1'} = 405$ cm^{-1}).[122] Hence, the strain and doping lines separate the ($\omega_{E'}$; $\omega_{A1'}$) plane in four regions corresponding to different types of doping and strain of 1L MoS_2, with the tensile (compressive) strain and the n-type (p-type) doping directions indicated by the black and red arrows, respectively. The parallel red and black dashed lines in the plot serve as guide for the eye to quantify the strain and doping values.

© 2024 The Author(s). Advanced Functional Materials published by Wiley-VCH GmbH

Figure 8. a) AFM morphology of 1L MoS_2 partially covering the surface of a flat Au film deposited by sputtering on SiO_2 with a Ni adhesion layer. b) Histogram of height values from the AFM analysis, indicating a very conformal coverage of 1L MoS_2 on Au. c) Cross-section HAADF-STEM image of the 1L MoS_2 on Au, showing a Mo—Au distance in a range between 4.0 and 4.4 Å. d) Raman spectra of MoS_2 with different thicknesses (1L, 2L, few layers, and bulk) exfoliated on Au (continuous lines) and transferred on Al_2O_3/Si (dashed lines). PL spectra collected on 1L, few layers, and bulk MoS_2 e) exfoliated on Au and f) transferred onto A_2O_3/Si substrate. (a)–(c) Adapted with permission.[118] Copyright 2023, Elsevier. (d)–(f) Adapted with permission.[119] Copyright 2021, American Institute of Physics.

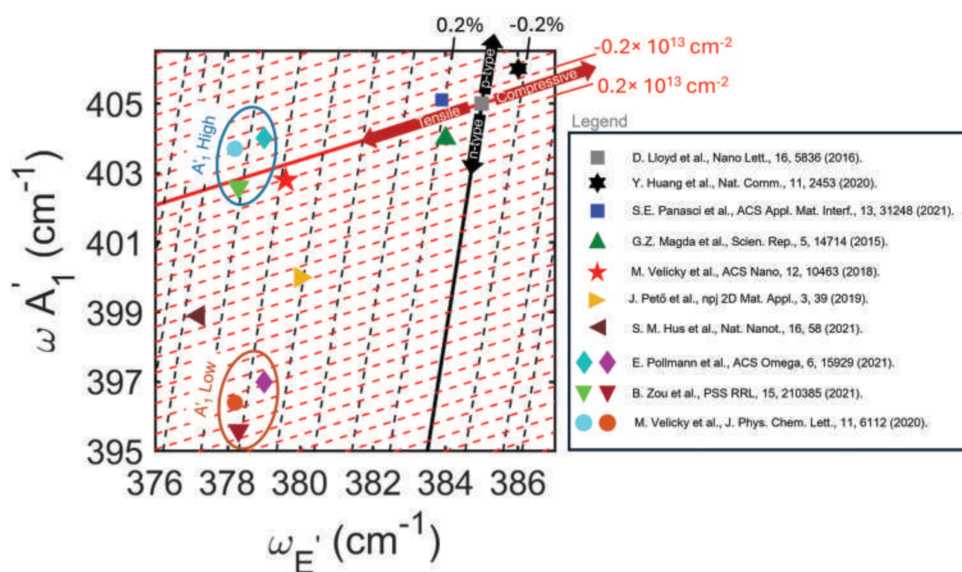

Figure 9. Correlative plot of the E′ and A'_1 Raman modes for 1L MoS_2 samples exfoliated on Au surfaces, with the experimental data points extracted from different literature papers, as indicated in the legend.

© 2024 The Author(s). Advanced Functional Materials published by Wiley-VCH GmbH

16163028, 0, Downloaded from https://onlinelibrary.wiley.com/doi/10.1002/adfm.202414532 by CNR Bologna, Wiley Online Library on [25/11/2024]. See the Terms and Conditions (https://onlinelibrary.wiley.com/terms-and-conditions) on Wiley Online Library for rules of use; OA articles are governed by the applicable Creative Commons License

In Figure 9, the spread between experimental points taken by different literature works clearly reflects the variability of strain and doping for 1L MoS_2 exfoliated on Au substrates, mostly depending on the Au surface preparation and morphology. The cases when the A'_1 exhibits a splitting into A'_1(H) and A'_1(L) are indicated by the blue and red ellipses.

Noteworthy, in most of the reports, Au supported 1L MoS_2 exhibits a tensile strain, with values ranging from ≈0.2%[87,124] to ≈1.4%,[111,112,115] whereas a small compressive strain ≈−0.2% is reported by few authors.[99] Such a variability of strain can be ascribed to the occurrence of different atomic-scale configurations of the MoS_2/Au interfaces, as illustrated by Sarkar et al.[125] using first-principle calculations of the MoS_2/Au(111) system. Different surface roughness of the Au substrate can play a crucial role on the strain of the MoS_2 membrane. Regarding doping of Au-supported MoS_2, most of the literature data indicate a relatively small (from 2 to 4×10^{12} cm^{-2}) p-type or n-type doping, whereas a larger spread in the doping values is deduced from some literature works, especially in the cases when a splitting of the A'_1 is observed.

4. Transfer of Large-Area Monolayer MoS_2 Membranes Obtained by Metal-Assisted Exfoliation

As previously discussed, the Au-assisted exfoliation allows to obtain large-area (mm^2 to cm^2) MoS_2 membranes, mostly composed by a monolayer, with high repeatability. However, device applications of as-exfoliated membranes in contact with the Au substrates are very limited. As an example, optoelectronic applications of 1L MoS_2 on Au are hampered by the significant quenching of photoluminescence signal due to charge-transfer at MoS_2/Au interface,[87,111,126] whereas MoS_2 field-effect transistors (FETs) applications are limited by the presence of the conductive Au layer underneath the 2D semiconductor channel. For these reasons, the transfer of exfoliated MoS_2 from Au to an insulating or semiconducting substrate is a necessary step for devices realization.

This section provides an overview of the three main methods demonstrated so far for the Au-assisted exfoliation and transfer of MoS_2 membranes. As illustrated in **Figure 10**, these methods can be grouped in two main categories, depending on how the interface between the bulk MoS_2 and Au is obtained, i.e., the mechanical pressure between MoS_2 and a predeposited Au film (a,b), or the direct physical vapor deposition of Au on MoS_2 surface (c).

4.1. Mechanical Adhesion between Bulk MoS_2 and Au Surfaces

1L MoS_2 exfoliation by mechanical adhesion between bulk MoS_2 and an Au surface can be implemented in different ways.

A first method (Method 1), illustrated in Figure 10a, consists of the following steps:

1) PVD deposition of an Au thin film with an adhesion layer (typically Ti or Ni) on a substrate, such as SiO_2/Si;
2) pressing the bulk MoS_2 stamp on the Au surface to exfoliate 1L MoS_2 membrane;
3) coating the 1L MoS_2/Au surface with a polymer protective layer (such as PMMA) and a thermal release tape (TRT);
4) etching of the Au film to release the TRT/PMMA/1L MoS_2 stack from the substrate;
5) transfer to the target substrate by pressing the stack, and releasing the TRT by heating at 100–150 °C on a hot plate; and
6) final removal of the polymer protective layer by solvents (e.g., acetone for PMMA).

An alternative way (Method 2) to implement this approach consists in the realization of an "Au adhesive tape,"[87] which can be pressed on the surface of the bulk MoS_2 crystal, as illustrated in Figure 10b. This method consists of the following steps:

1) PVD deposition (evaporation or sputtering) of an Au film (without any adhesion layer) on an Si surface and, subsequently, spin-coating a polymer layer (e.g., PMMA) on the Au surface;
2) pressing a TRT tape on the PMMA surface and peeling-off the PMMA/Au membrane from the Si substrate, thanks to the low adhesion of Au on Si;
3) pressing the freshly peeled Au surface on a bulk MoS_2 sample to exfoliate a 1L MoS_2 membrane;
4) pressing the TRT/polymer/Au/1L MoS_2 stack on the target substrate and releasing the TRT by heating on a hot plate; and
5) sequentially removing PMMA in acetone, and Au etching in a KI/I_2 solution.

The main advantage of these methods is the possibility to obtain, in principle, a very sharp vdW interface between Au and MoS_2, as illustrated in the schematic and cross-sectional TEM image in Figure 10d. However, as already discussed in Section 3, to achieve a high monolayer exfoliation yield, the as-deposited Au surface must be very flat and the accumulation of contaminations due to exposure to air must be avoided.

4.2. PVD Deposition of Au on Bulk MoS_2

An alternative approach (Method 3),[128,129] schematically illustrated in Figure 10c, is based on the following steps:

1) The direct PVD, i.e., evaporation or sputtering, of a thin Au film directly on the bulk MoS_2 surface;
2) pressing a TRT on the freshly deposited Au film, followed by the exfoliation of the Au/MoS_2 stack. Typically, an ultrasonication process is employed to remove the thicker parts of the exfoliated MoS_2 and leave an extended 1L MoS_2 on Au;
3) pressing of the TRT/Au/1L-MoS_2 stack on the target substrate;
4) releasing the TRL tape on a hot plate at a temperature of 100–150 °C; and
5) etching of the Au film in a solution of KI/I_2 at room temperature for few minutes, followed by a thorough cleaning in H_2O, to leave an extended 1L MoS_2 on the target substrate.

By using this approach, Desai et al.[128] demonstrated the exfoliation of 1L MoS_2 flakes with areas 10^4 times larger compared to those obtained by the conventional mechanical exfoliation using

© 2024 The Author(s). Advanced Functional Materials published by Wiley-VCH GmbH

16163028, 0, Downloaded from https://onlinelibrary.wiley.com/doi/10.1002/adfm.202414532 by CNR Bologna, Wiley Online Library on [25/11/2024]. See the Terms and Conditions (https://onlinelibrary.wiley.com/terms-and-conditions) on Wiley Online Library for rules of use; OA articles are governed by the applicable Creative Commons License

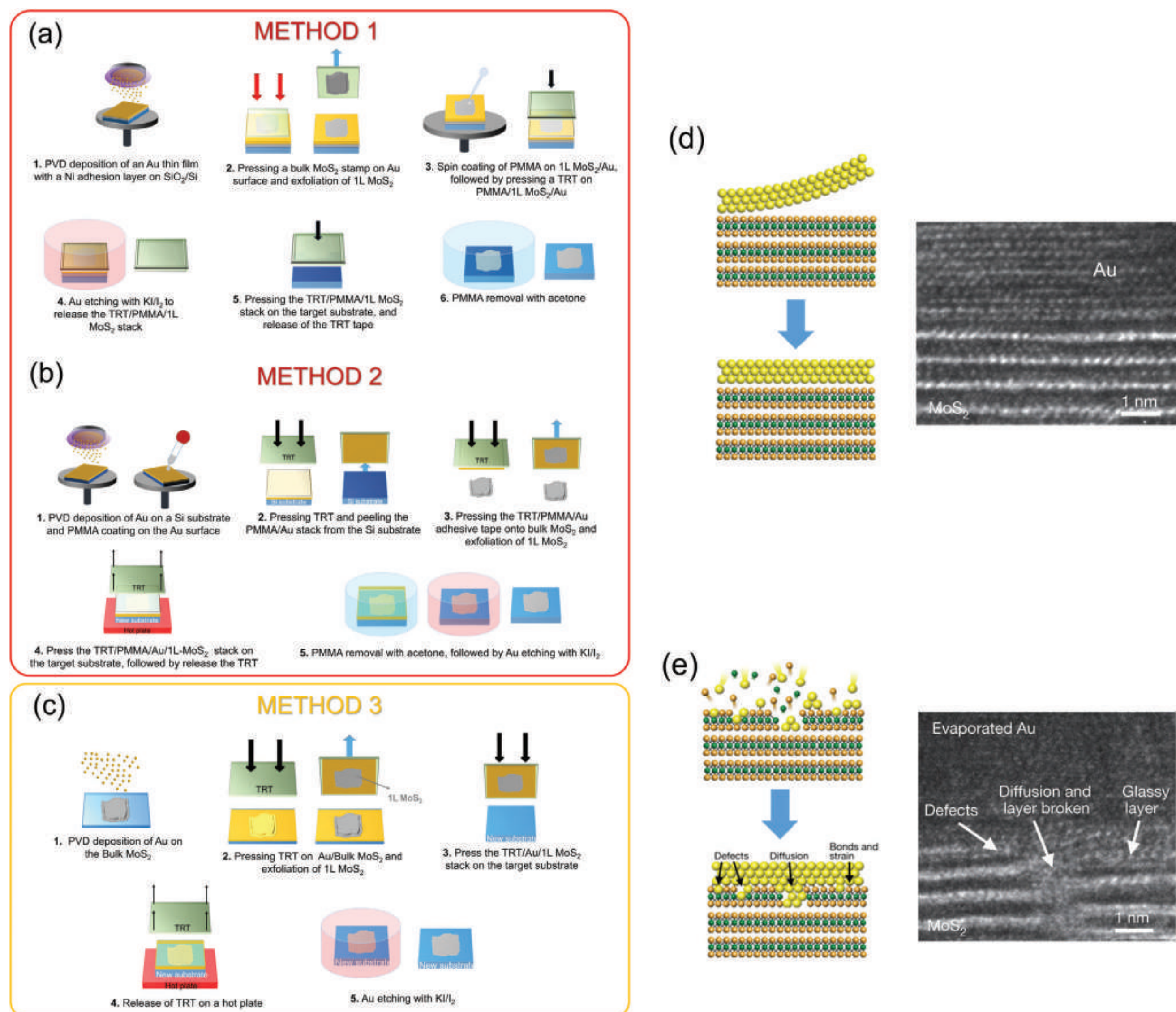

Figure 10. Illustration of the three main methods for Au-assisted exfoliation and transfer of large-area 1L MoS_2 membranes, grouped in two categories, depending on how the interface between the bulk MoS_2 and Au is obtained: a) in Method 1 and b) Method 2 mechanical pressure between bulk MoS_2 and predeposited Au; c) in Method 3 direct PVD of Au on bulk MoS_2 surface. d) Schematic and cross-sectional TEM image of the vdW interface obtained by pressing Au on MoS_2. e) Illustration of possible surface damage occurring during Au PVD on bulk MoS_2, and cross-sectional TEM image of the Au/MoS_2 interface. (d) and (e) Adapted with permission.[127] Copyright 2018, Springer Nature.

an adhesive tape. PVD of Au allows a nearly conformal coverage of the bulk MoS_2 surface. However, a main issue related of this approach is the possible surface damage induced during deposition by energetic Au atoms, which can diffuse inside MoS_2 crystal introducing vacancies and extended defects,[127,130] as illustrated in the schematic and in the cross-sectional TEM image in Figure 10e. These defects can ultimately affect the structural and electrical quality of the exfoliated 1L MoS_2 membrane. Hence, an accurate optimization of the main PVD parameters is necessary to minimize these phenomena[131] when adopting this method for Au-assisted exfoliation.

Table 1 below reports a literature survey on the application of the three transfer methods illustrated in Figure 10. In particular, the type of exfoliated 2D monolayers, the polymers used in the transfer, the Au etching and polymer removal approaches are listed. Furthermore, the relevant electrical properties of transferred 1L-MoS_2 measured using transistor devices (i.e., the field-effect mobility and/or I_{on}/I_{off} current ratio) are reported for benchmarking. Here, it is worth noting that although all the three "Au-assisted exfoliation and transfer methods" make use of polymers or TRT for the films' manipulation and transfer, a direct contact between the polymer and 1L-MoS_2 occurs only in Method 1. The most used polymer in Method 1 is spin-coated PMMA on 1L-MoS_2, which is known to leave many residues even after removal with acetone.[132,133] As an alternative less-contaminating polymer, Sahu et al.[134] recently employed a ready-to-use poly(dimethylsiloxane) (PDMS) stamp for dry transfer of 1L-MoS_2/Au. Finally, Heyl et al.[34] proposed a modified

© 2024 The Author(s). Advanced Functional Materials published by Wiley-VCH GmbH

16163028, 0, Downloaded from https://onlinelibrary.wiley.com/doi/10.1002/adfm.202414532 by CNR Bologna, Wiley Online Library on [25/11/2024]. See the Terms and Conditions (https://onlinelibrary.wiley.com/terms-and-conditions) on Wiley Online Library for rules of use; OA articles are governed by the applicable Creative Commons License

16163028, 0, Downloaded from https://onlinelibrary.wiley.com/doi/10.1002/adfm.202414532 by CNR Bologna, Wiley Online Library on [25/11/2024]. See the Terms and Conditions (https://onlinelibrary.wiley.com/terms-and-conditions) on Wiley Online Library for rules of use; OA articles are governed by the applicable Creative Commons License

Table 1. Literature survey on the application of the transfer methods, including information on the type of exfoliated 2D monolayers, the polymers used in the transfer, the Au etching and polymer removal approaches, and relevant electrical properties of transferred 1L-MoS_2 measured using transistor devices.

Exfoliation and transfer method	Exfoliated 2D monolayers	Polymer used	Au etching	Polymer removal	MoS_2 electrical properties	Refs.
1	>40 2D materials	PMMA	KI/I_2 + DI water (3 times)	Acetone	$\mu \approx 30$ cm^2 V^{-1} s^{-1} $I_{on}/I_{off} \approx 10^7$	[99]
1	MoS_2	Polymer-free	$FeCl_3$ (12 h) + KI/I_2 (30 min)	–	$\mu \approx 8.9$ cm^2 V^{-1} s^{-1} $I_{on}/I_{off} \approx 10^5$	[34]
1	MoS_2, WS_2, $MoSe_2$, WSe_2, $PtSe_2$, graphene	PDMS	KI/I_2 + KCl+DI water (3 times)	–	$\mu \approx 0.86$ cm^2 V^{-1} s^{-1}	[134]
2	MoS_2	PMMA	KI/I_2 + DI water	Acetone + IPA (10 min)	$\mu \approx 2.3$ cm^2 V^{-1} s^{-1}	[87]
2	MoS_2, WS_2, $MoSe_2$, WSe_2	PC and PVA	–	–	$\mu \approx 63$ cm^2 V^{-1} s^{-1} $I_{on}/I_{off} \approx 10^8$	[83]
3	MoS_2	TRT	KI/I_2 (4 min) + Acetone/IPA (10 min)	Thermal release of the TRT	$\mu \approx 26$ cm^2 V^{-1} s^{-1}	[128]
3	MoS_2, WS_2	AZ 4620 photoresist	KI/I_2 + DI water	Acetone (4 h)	$I_{on}/I_{off} \approx 10^3$–$10^7$	[81]
3	MoS_2	TRT	KI/I_2 + DI water	Thermal release of the TRT	$\mu \approx 0.5$–20 cm^2 V^{-1} s^{-1} $I_{on}/I_{off} \approx 10^4$–$10^6$	[129]

(i.e., polymer-free) version of the transfer Method 1, where the gold substrate was used for exfoliation as well as for transfer. In this approach, 1L-MoS_2 exfoliation is carried out on a thick (200 nm) gold film deposited on an 800 nm sacrificial copper layer supported on an epoxy/glass substrate. Chemical etching of the Cu layer (in $FeCl_3$) results in a floating Au/2D membrane, which is subsequently transferred on the target substrate, followed by final etching (using KI/I_2) of the gold film.

Interestingly, the results of the literature survey reported in Table 1 show, for all the three methods, a significant spread of measured mobility values (i.e., from 0.86[134] to 30 cm^2 V^{-1} s^{-1}[99] for Method 1, from 2.3[87] to 63 cm^2 V^{-1} s^{-1}[83] for Method 2, and from 0.5[129] to 26 cm^2 V^{-1} s^{-1}[128] for Method 3), with maximum values comparable to those obtained from classic scotch-tape exfoliation.[17,19] Hence, besides possible polymer residues, other factors involved in the transferring process, including adhesion on the target substrate, cracks and strain in the 1L-MoS_2 membrane, can influence the final electrical performances. An ultimate approach to avoid any polymer contamination of exfoliated 1L-MoS_2 on gold would be coating its surface with a thin high-κ insulating film (deposited by ALD) before the transfer process, as recently proposed by Schilirò et al.[135] Besides preventing the contact with polymers or TRT, this high-κ encapsulation will result in a strong improvement of MoS_2 carrier mobility for transistors applications.[17]

5. Devices Applications and Advanced Processing

5.1. Memristors Based on 1L MoS_2/Au Junctions

A recently demonstrated device concept based on the 1L MoS_2/Au system is represented by the metal/MoS_2/Au memristor, a nonvolatile resistive switching memory device, very promising for ultradense data storage and neuromorphic computing systems.[117,136–140] **Figure 11**a,b shows a schematic illustration and an optical microscopy image of such device structure, where 1L MoS_2 is sandwiched between two Au electrodes, whereas the current–voltage characteristics in Figure 11c clearly illustrate the bipolar memristor behavior, i.e., the switching from a high resistance state (HRS) to a low resistance state (LRS) by applying a proper positive SET voltage between the two electrodes, and the switching back from the LRS to the HRS by applying a negative RESET voltage.[138] More recently, Hus et al.[117] demonstrated the crucial role of atomic scale defects (specifically sulfur vacancies) of 1L MoS_2 in the resistive switching behavior of 1L MoS_2/Au memristors by scanning tunneling microscopy (STM) and spectroscopy (STS) in ultrahigh vacuum.

Starting from high-quality and large-area 1L MoS_2 as-exfoliated on Au, the authors intentionally increased the density of sulfur vacancies by an annealing process at 400 °C for several hours in ultrahigh vacuum conditions. Atomic resolution STM images revealed a typical diode-like behavior of the Au tip/1L MoS_2/Au–substrate junction in the defects-free MoS_2 areas, as illustrated in Figure 11d–f. On the other hand, the occurrence of a resistive switching behavior from an HRS to an LRS was demonstrated on the sulfur vacancy sites, identified by STM imaging (Figure 11g,h). Specifically, starting from an "empty" S vacancy (Figure 11h) and applying a positive tip bias of ≈1.8 V, the switching from the LRS to the HRS (SET event) was associated with the filling of the vacancy with a substitutional Au atom (Figure 11i,j). The switching back from the LRS to the HRS by applying a negative tip bias of −1.1 V (RESET event) was instead associated to the restoring of the empty S vacancy (Figure 11k,l).

5.2. Photodetectors

Owing to its sub-nanometer thickness and ≈1.9 eV direct bandgap, 1L MoS_2 has been considered since the early studies for optoelectronic devices, including ultrasensitive photodetectors,[19] phototransistors,[21,22] or photovoltaic cells.[23] As a matter of fact, most of these high-performance early

© 2024 The Author(s). Advanced Functional Materials published by Wiley-VCH GmbH

16163028, 0, Downloaded from https://onlinelibrary.wiley.com/doi/10.1002/adfm.202414532 by CNR Bologna, Wiley Online Library on [25/11/2024]. See the Terms and Conditions (https://onlinelibrary.wiley.com/terms-and-conditions) on Wiley Online Library for rules of use; OA articles are governed by the applicable Creative Commons License

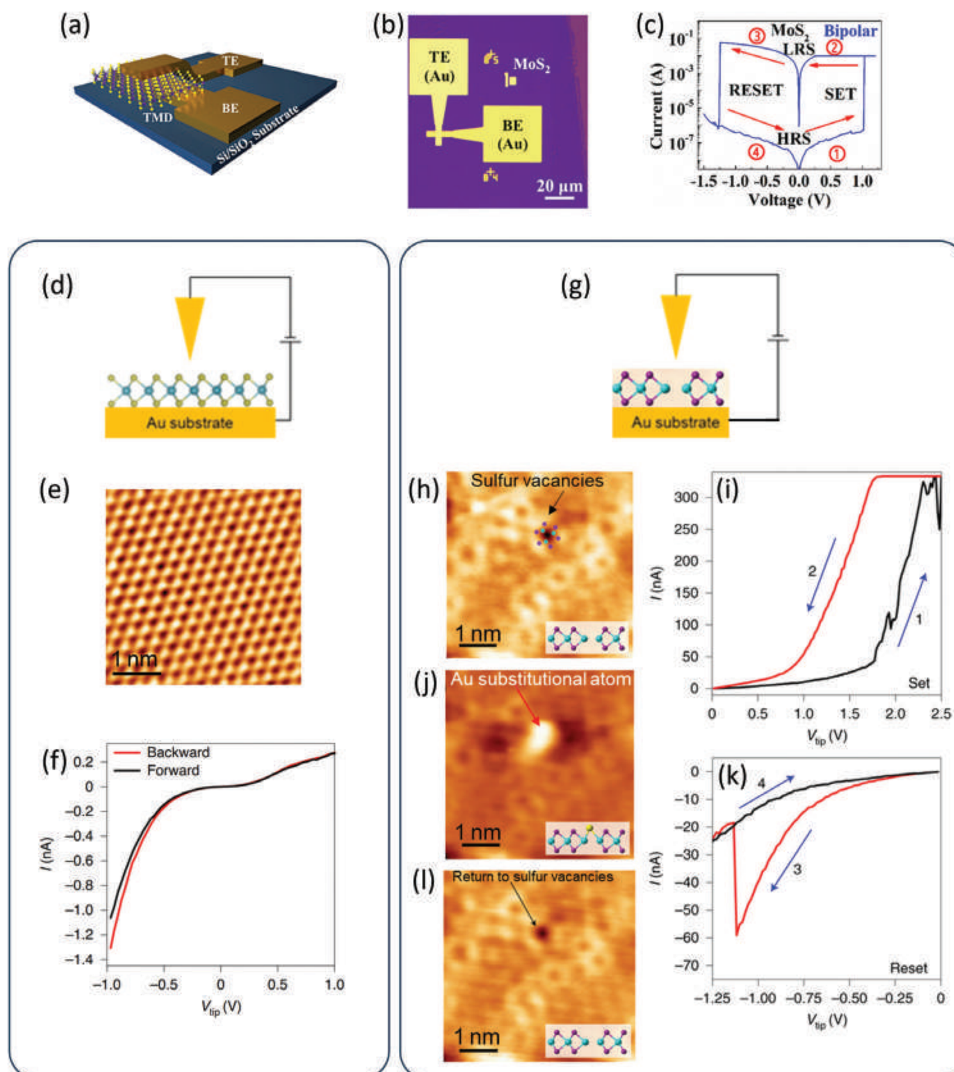

Figure 11. a) Schematic illustration and b) optical microscopy of an Au/1L MoS_2/Au memristor. c) Current–voltage characteristics of the device illustrating the bipolar memristor behavior. d) Schematic of the STM setup used to characterize the defects-free MoS_2 on Au. e) Corresponding atomic-scale STM image and f) local *I–V* characteristics of a defects-free region of 1L MoS_2 exfoliated on Au, showing a typical rectifying behavior at the Au tip/1L MoS_2/Au substrate junction. g) Schematic of the STM setup used to characterize an S vacancy defect in 1L-MoS_2 on Au. h) Corresponding atomic-scale STM characterization of an S vacancy defect in 1L MoS_2 on Au. i) Local current–voltage characteristics on the defect's region, showing the transition from a low resistance state (LRS) to a high resistance state (HRS) by the application of a positive tip bias of ≈1.8 V. j) STM image after the "set event" showing the presence of a substitutional Au atom in the S vacancy site. k) Local current–voltage characteristics showing the occurrence of the "reset event" by application of a negative tip bias and l) STM image acquired after the reset event, showing the restoring of S vacancy defect. (a)–(c) Adapted with permission.[138] Copyright 2018, American Chemical Society. (d)–(l) Adapted with permission.[117] Copyright 2021, Springer Nature.

demonstrators have been realized using small-size high-crystalline quality MoS_2 flakes obtained by mechanical exfoliation from bulk crystals. Whereas CVD and MOCVD techniques represent nowadays the most suitable approaches for future industrial applications, large-area membranes produced by Au-assisted exfoliation may be useful to fabricate devices arrays for benchmarking purposes.

Recently, high-performance photodetectors have been demonstrated using large-area 1L MoS_2 exfoliated on Au and transferred onto SiO_2/Si substrates,[134] as illustrated in **Figure 12a–c**. Figure 12d reports the drain–source current–voltage (I_{ds}–V_{ds}) characteristics of the phototransistor in the dark and under illumination, using a focused laser beam ($\lambda = 514.5$ nm) of different illumination power densities in the range 2.5–63.6 μW cm^{-2}. The linearity and symmetry of the I_{ds}–V_{ds} curves demonstrate the formation of ohmic contacts onto MoS_2. Furthermore, an increase of I_{ds} by several orders of magnitude as a function of laser power is demonstrated. Figure 12e shows the time-dependent photoresponse of the phototransistor (at a source–drain bias V_{ds} = 1 V and backgate bias V_g = 0 V) under incident laser pulses at different power densities, demonstrating rise and decay times and a dependence of the maximum photocurrent on the power density comparable to those of similar devices fabricated with small mechanically exfoliated flakes. Similarly, the values of

 © 2024 The Author(s). Advanced Functional Materials published by Wiley-VCH GmbH

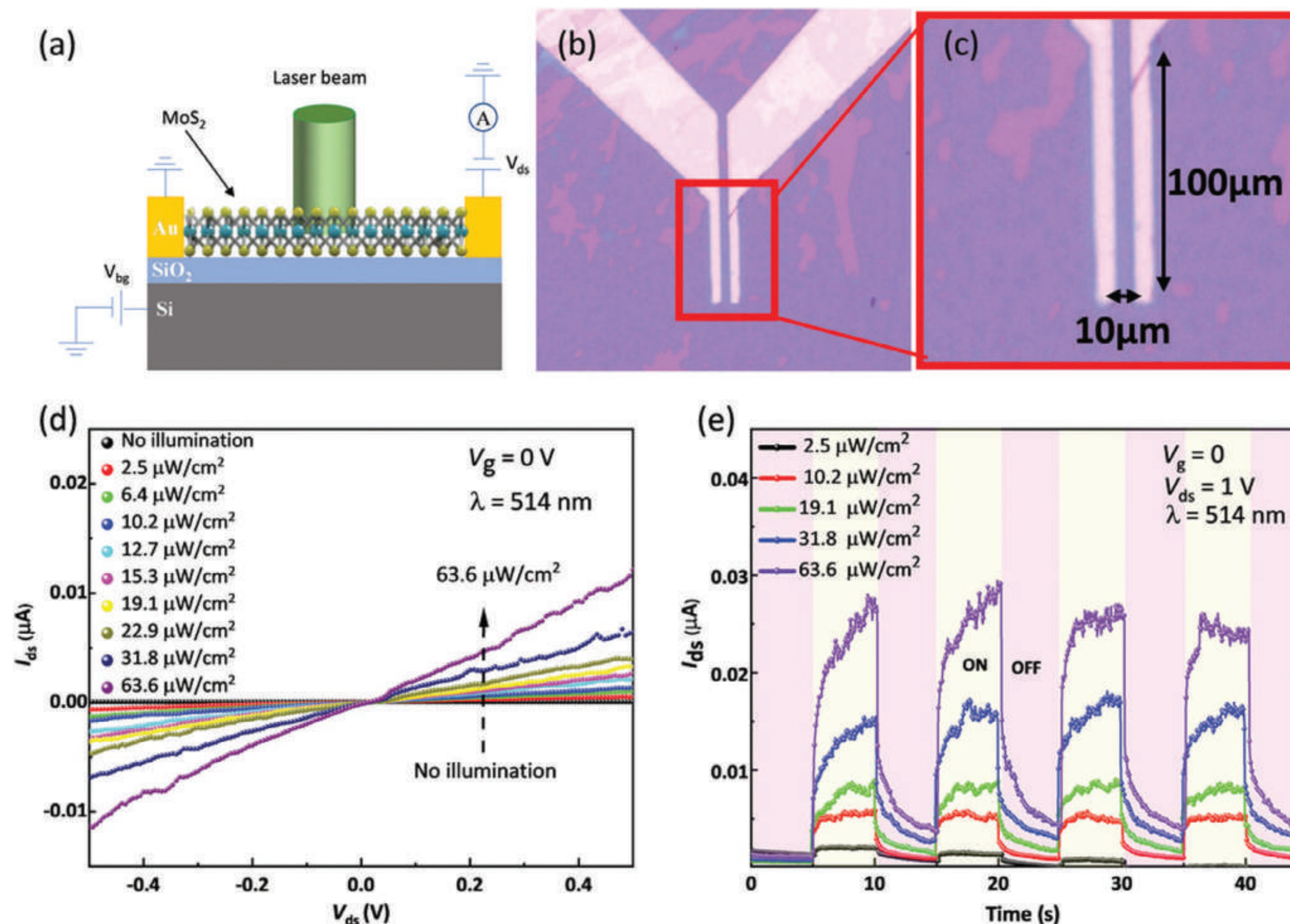

Figure 12. a) Schematic and b,c) optical images of a photodetector fabricated using large-area 1L MoS_2 exfoliated on Au and transferred on an SiO_2/Si substrate. d) Device photoresponse in the dark and under illumination with a laser source (λ = 514.5 nm) at different power densities (from 2.5 to 63.6 mW cm^{-2}) with V_{ds} = 1 and V_{bg} = 0 V. e) Time-dependent photoresponse for different illumination power densities. Figures reproduced and adapted with permission.[134] Copyright 2023, Wiley.

photodetector responsivity, i.e., the ratio between the photocurrent and the power of the light ($R = I_{ph}/P$), are comparable to those obtained by mechanical exfoliated MoS_2-based devices at similar bias and illumination power. As a further demonstration of the high-quality (i.e., low defectivity) of the Au-exfoliated and transferred membrane, the device performances proved to be stable, even without any passivation, after five months from the fabrication.[134]

5.3. Field-Effect Transistors

Besides optoelectronic devices, FETs represent one of the main application fields of MoS_2 and other TMDs. As a matter of fact, MoS_2 on Au is not a suitable system to implement FETs, due to the presence of the conductive metal substrate, which typically represents a preferential parallel conduction path with respect to the MoS_2 channel. To circumvent this issue, Huang et al.[99] recently fabricated an ionic-liquid top-gated FET using 1L MoS_2 exfoliated onto an ultrathin and discontinuous Au (1.5 nm)/Ti (0.5 nm) film on an SiO_2/Si substrate, as illustrated in **Figure** 13a. In this case the sheet resistance of the Au/Ti film was significantly higher than the one of 1L MoS_2. Hence, the channel conductance of the 2D semiconductor was very efficiently modulated by an ionic liquid top-gate, showing remarkable performances, such as a subthreshold swing (SS) ≈ 100 mV dec^{-1} and a mobility between 22.1 and 32.7 cm^2 V^{-1} s^{-1} (see Figure 13b). Obviously, this ionic liquid gated FET device simply served to demonstrate the excellent electronic properties of as-exfoliated MoS_2 on Au, but it is not suitable for practical applications. On the other hand, the commonly adopted backgated MoS_2 FETs structure (see schematic in Figure 13c) requires the transfer of 1L MoS_2 on a dielectric substrate.

Figure 13d,e shows the I_{ds}–V_G transfer characteristics and the I_{ds}–V_{ds} output characteristics of a long channel (L = 20 µm, W = 3 µm) MoS_2 FET fabricated by transfer of Au-exfoliated 1L MoS_2 onto an SiO_2 (50 nm)/Si substrate. This prototype showed a good on/off ratio of about 10^5–10^6 and a field-effect mobility ≈26 cm^2 V^{-1} s^{-1}, comparable with the reported values for backgated FETs fabricated using mechanically exfoliated micrometer area MoS_2 flakes. As a matter of fact, the large lateral extension of transferred Au-exfoliated 1L MoS_2 membranes allows to

© 2024 The Author(s). Advanced Functional Materials published by Wiley-VCH GmbH

16163028, 0, Downloaded from https://onlinelibrary.wiley.com/doi/10.1002/adfm.202414532 by CNR Bologna, Wiley Online Library on [25/11/2024]. See the Terms and Conditions (https://onlinelibrary.wiley.com/terms-and-conditions) on Wiley Online Library for rules of use; OA articles are governed by the applicable Creative Commons License

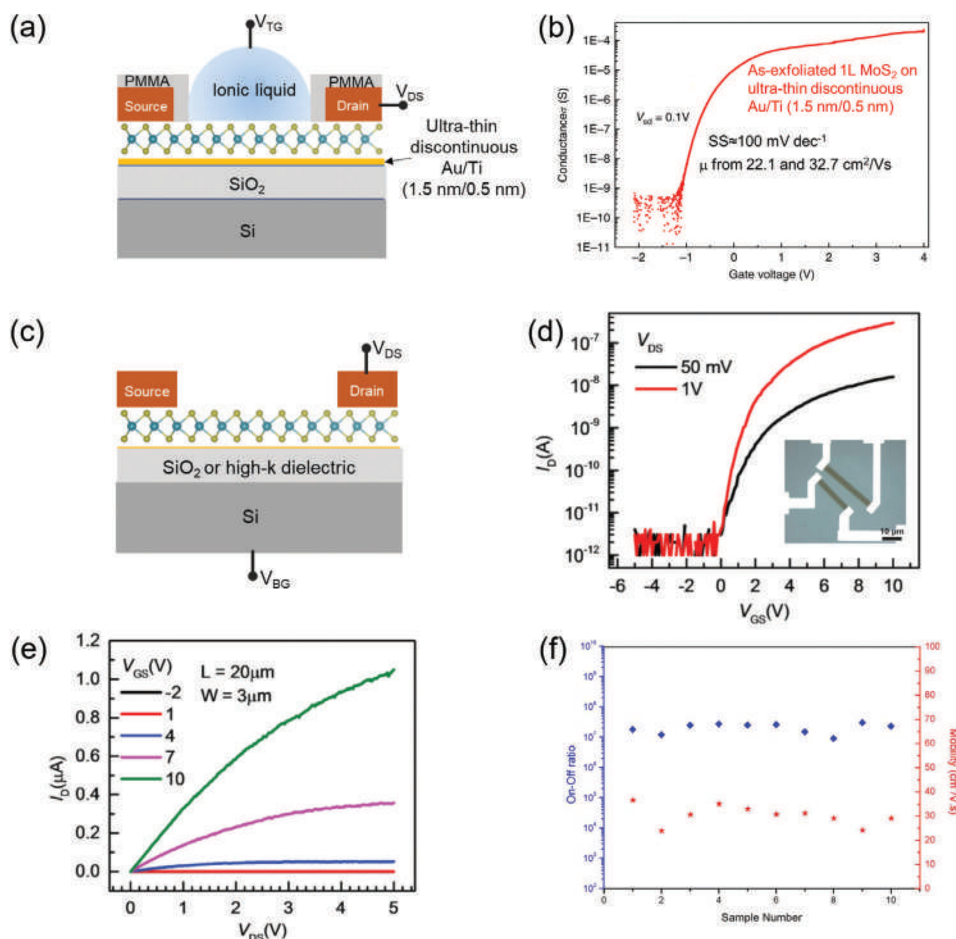

Figure 13. a) Schematic of an ionic-liquid top-gated FET fabricated with as-exfoliated 1L MoS_2 on an ultrathin discontinuous Au/Ti (1.5 nm/0.5 nm) film. b) Transfer characteristic of this device, demonstrating the excellent electronic quality of as-exfoliated 1L MoS_2. c) Schematic of a back-gated FET fabricated using large-area 1L MoS_2 exfoliated on Au and transferred onto an insulating substrate. d,e) Typical transfer and output characteristics of the back-gated device. f) Statistics of the on/off intensity ratio (blue) and mobility (red) on an array of 1L MoS_2 FETs. (b) and (f) adapted with permission,[99] Copyright 2020, Springer Nature, and (d) and (e) adapted with permission.[128,135] Copyright 2016, Wiley.

fabricate arrays of backgated FETs[99] and to perform statistic evaluation on the uniformity of the main electrical parameters, such as the mobility (in the range between 20 and 30 $cm^2 V^{-1} s^{-1}$) and on/off ratio (between 10^7 and 10^8), as illustrated in Figure 13f.

5.4. Advanced Processing for 2D Transistors: High-κ Dielectrics Integration onto Au-Exfoliated 1L MoS_2

One of the key process steps for 2D semiconductors-based transistors is represented by the integration of high-κ insulating films on their surface, to be used as a passivation against humidity and contaminations from the environment and/or as top-gate dielectrics for local modulation of channel conductivity. The beneficial effects of the encapsulation of 1L MoS_2 with high-κ dielectrics were demonstrated since the early reports on MoS_2 FETs, by showing a large improvement of the field-effect mobility (up to ≈200 $cm^2 V^{-1} s^{-1}$) after deposition of Al_2O_3 or HfO_2 films on mechanically exfoliated flakes.[141–143] Such mobility improvement was ascribed to a strong reduction of the Coulomb scattering of MoS_2 electrons by charged impurities ($V_{Coul} \propto \frac{Q}{k_0 k_r}$), owing to the higher dielectric permittivity κ_r of the surrounding ambient,[141,142] and/or to a reduction of the electron/phonon interactions.[144]

Currently, atomic layer deposition (ALD) is the method of choice for the growth of ultrathin high-κ dielectric films in micro- and nanoelectronics. In a typical ALD process, the initiation of the layer-by-layer growth on a substrate requires the presence of a large density of surface dangling bonds. As a matter of fact, this nucleation step is hindered on the dangling bonds-free sp^2 surface of 2D materials, typically resulting in a highly inhomogeneous surface coverage during the early stages of the ALD process. To circumvent this inherent limitation, different surface preparation approaches of 2D materials have been explored so far to promote ALD growth. These include the coating of 2D materials surfaces with thin seed layers (spin-coated polymer thin films,[145–147] self-assembled monolayers,[148,149] or PVD deposited metal or metal oxide films[150,151]) or the prefunctionalization of the 2D materials surface, e.g., by soft plasma treatments, to intentionally introduce dangling bonds.[152] Recently, similar approaches have also been used for the ALD growth on transferred large-area 1L MoS_2 membranes produced by Au-assisted

© 2024 The Author(s). Advanced Functional Materials published by Wiley-VCH GmbH
16163028, 0, Downloaded from https://onlinelibrary.wiley.com/doi/10.1002/adfm.202414532 by CNR Bologna, Wiley Online Library on [25/11/2024]. See the Terms and Conditions (https://onlinelibrary.wiley.com/terms-and-conditions) on Wiley Online Library for rules of use; OA articles are governed by the applicable Creative Commons License

16163028, 0, Downloaded from https://onlinelibrary.wiley.com/doi/10.1002/adfm.202414532 by CNR Bologna, Wiley Online Library on [25/11/2024]. See the Terms and Conditions (https://onlinelibrary.wiley.com/terms-and-conditions) on Wiley Online Library for rules of use; OA articles are governed by the applicable Creative Commons License

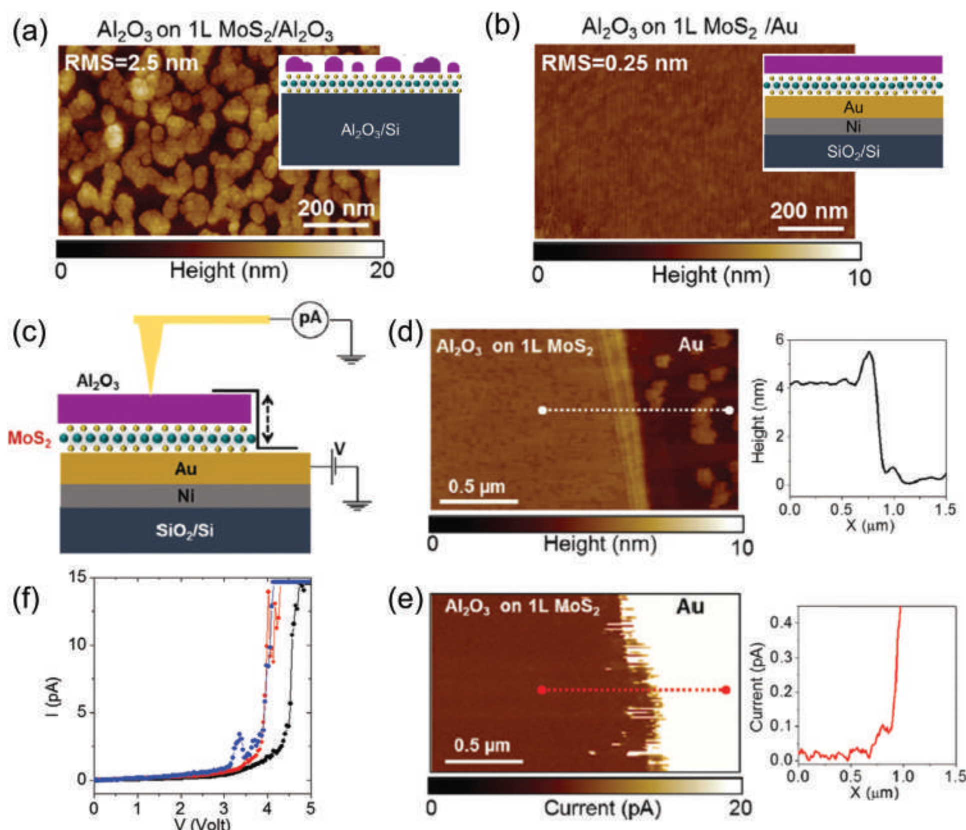

Figure 14. AFM images and schematic cross sections illustrating the very different uniformity of Al_2O_3 thin films deposited under identical ALD conditions on a) 1L MoS_2/Al_2O_3/Si and b) 1L-MoS_2/Au. c) Schematic of the C-AFM setup used to evaluate the thickness and insulating properties of the thin Al_2O_3 film deposited on 1L MoS_2/Au. d) Morphology map with a height line profile and e) current map with a current line profile, collected in a patterned Al_2O_3/MoS_2 region. An Al_2O_3 thickness of ≈3.6 nm and excellent insulating properties are deduced from these analyses. f) Local current–voltage (I–V_{tip}) characteristics at different positions of the Al_2O_3 film, from which a breakdown field of 10–12 MV cm^{-1} has been estimated. Figures reproduced and adapted with permission from ref. [135] Copyright 2021, Wiley.

exfoliation. As an example, the encapsulation with a thin Al film (≈1 nm) naturally oxidized air, followed by thermal ALD of 10 nm Al_2O_3, proved to be very effective in improving the electrical performances of back-gated FETs with a large-area 1L MoS_2 channel, achieving field-effect mobility values in the range of 40 cm^2 V^{-1} s^{-1}.[129]

As a matter of fact, the above-mentioned approaches to promote ALD growth exhibit several limitations, as they can affect the carrier mobility of MoS_2 (e.g., in the case of plasma pretreatments) or the interface quality of the dielectric films and their equivalent oxide thickness (e.g., in the case of predeposited seeding layers). Hence, the direct ALD growth of high-κ dielectrics on MoS_2, without any seed layers and prefunctionalization processes, is highly desirable, especially for the integration of ultrathin (few nm) top-gated dielectrics in ultrascaled 2D FETs.

Recently, Schilirò et al.[118,135] demonstrated the direct ALD growth of ultrathin (<5 nm) and uniform high-κ dielectric films (Al_2O_3, HfO_2) with excellent insulating quality on the surface of as-exfoliated 1L MoS_2 on Au. **Figure** 14a,b shows a comparison between the morphologies of Al_2O_3 thin films deposited under identical thermal ALD conditions (80 cycles with TMA and H_2O precursors at a temperature of 250 °C) on 1L MoS_2 transferred onto Al_2O_3/Si (a) and on as-exfoliated 1L MoS_2 on Au (b). While a very inhomogeneous Al_2O_3 coverage was obtained on 1L MoS_2 supported by Al_2O_3/Si, consistently with the typically reported growth on 2D materials surfaces,[143] a very uniform and flat Al_2O_3 coverage was achieved on 1L MoS_2/Au. The enhanced Al_2O_3 nucleation on Au-supported 1L MoS_2 was ascribed to a higher reactivity with ALD precursors, originating from the strain of 1L MoS_2 membrane and from electrostatic fields generated by dipoles at MoS_2/Au interface. Similarly, an enhanced ALD growth has been reported in the case of CVD-grown graphene on metals (Ni, Cu), due to charge dipoles present at graphene/metal interfaces,[153] and in the case of epitaxial graphene on 4H-SiC(0001), due to charged dangling bonds present at the buffer layer/4H-SiC interface.[154,155] Figure 14c–f reports a nanoscale resolution morphological and electrical characterization of ALD-grown Al_2O_3 on 1L MoS_2/Au by conductive atomic force microscopy (C-AFM). A uniform Al_2O_3 film with a thickness of ≈3.6 nm and excellent insulating properties was deduced from the topography and current map collected in a patterned Al_2O_3/MoS_2 region (Figure 14d,e). A breakdown electric field of 10–12 MV cm^{-1}, comparable with the state-of-the-art of high-κ dielectric film deposited by ALD on MoS_2,[156] was estimated from local I–V_{tip} analyses at different positions on Al_2O_3, as illustrated in Figure 14f.

© 2024 The Author(s). Advanced Functional Materials published by Wiley-VCH GmbH

These results demonstrate the highly beneficial role of the Au substrate for the ALD growth of uniform and ultrathin high-κ dielectrics on 1L MoS_2. An optimized transfer procedure of the high-κ/1L MoS_2 stack to insulating or semiconducting substrates will be the key for the extensive application of this approach for top-gated field-effect transistors fabrication.

6. Perspectives and Challenges

Starting from the promising results of Au-assisted 1L MoS_2 exfoliation, the monolayer-selective exfoliation on metal surfaces emerged as an universal approach for disassembling a variety of large-area 2D membranes from layered bulk crystals and reassembling them in 2D heterostructures.[88,99] **Figure 15a** shows a collection of optical images from a set of 40 different monolayer 2D materials exfoliated on an Au (2 nm)/Ti (2 nm) film onto SiO_2/Si substrate. These included, besides several TMDs, elemental 2D crystals (such as black P and black As), metal monochalcogenides (such as GaS), metal trichlorides (such as $RuCl_3$), and magnetic compounds (such as Fe_3GeTe_2).[99] Figure 15b reports an optical image of a cm^2 area $MoSe_2$/WSe_2 heterostructure on an SiO_2/Si substrate, fabricated by sequential Au-assisted exfoliation and transfer of the WSe_2 and $MoSe_2$ membranes. Noteworthy, the large-area and single-crystalline quality of the layers enabled the direct measurement of the energy bands of the $MoSe_2$/WSe_2 heterostructure by angle resolved photoemission spectroscopy (ARPES), as shown in Figure 15b bottom image.

In the last 15 years, the stacking of micrometer size mechanically exfoliated flakes has been used to demonstrate several 2D heterojunction device concepts, including p-n junctions obtained by the combination of differently doped 2D TMDs,[158,159] FETs and light emitting diodes (LEDs) entirely composed of 2D materials.[160] Starting from those early small-size prototypes, the sequential Au-assisted exfoliation and transfer approach would allow the fabrication of arrays 2D heterojunction devices on cm^2 areas, thus moving a step toward industrial needs. Furthermore, the high single crystal quality of the exfoliated monolayers may enable the realization of new concept devices, such as Moirè superlattice devices, based on rotationally misaligned 2D membranes with controlled twist angles (see the schematic illustration in Figure 15c).[157,161] These latter can be used to manipulate the electronic properties of crystalline solids through the formation of periodic potentials, involving unconventional superconductivity, conducting channels, and peculiar optoelectronic behavior.[161–164]

Despite the progresses in top-down 2D materials production by metal-assisted exfoliation discussed in this paper, many challenges still remain open to fully exploit the potential of this approach. Currently, the maximum size of the monolayer membranes that can be exfoliated on a gold surface is limited by the size (from few mm to cm), geometry and planarity of commercially available stamps of bulk mineral crystals. Efforts in upscaling the size of bulk crystals produced by synthetic methods, such as the flux method growth[165] and the chemical vapor transport (CVT) method,[166] will be crucial to allow a wider application of this exfoliation approach. Furthermore, a standardization of the metal-assisted-exfoliation protocols is required to achieve reproducible properties of 2D materials/metal interfaces, even in the model case of MoS_2 on Au. These protocols should include the following crucial aspects:

i) Control of surface roughness of Au or other metal films. This can be achieved by optimizing the PVD deposition conditions, in the case of these films deposited on a substrate, such as SiO_2/Si. The possibility of using metal foils, such as Au foils with ultraflat Au(111) surface prepared by flame annealing, can be considered to this purpose.
ii) Control of the ambient (glove-box, vacuum chamber) where as-prepared metal substrates are stored, to avoid the accumulation of contamination/moisture on their surface or oxidation (for some metal surfaces).
iii) Optimization/automation of the exfoliation procedure of 2D materials on the metal surface, and eventual post-exfoliation annealing.
iv) Optimization of the procedure to separate 2D materials from the metal surface. Besides the commonly adopted etching in a KI/I_2 solution in the case of TMDs exfoliated on Au thin films, proper etchants should be chosen in the case of other metal films to achieve optimal detachment of 1L MoS_2 without introducing defects. Furthermore, the possibility of adopting an electrolytic delamination approach[167] to separate large-area 1L MoS_2 membranes exfoliated on Au (or other metal foils) should be developed, as this method allows to reuse the metal substrate avoiding waste of precious material.
v) Optimization of the encapsulation of as-exfoliated 2D layers by ALD deposition of high-κ dielectrics, further developing early results on the enhanced ALD growth of Al_2O_3 and HfO_2 on Au-supported 1L MoS_2 membranes.[154,155]

7. Conclusion

In conclusion, we reviewed the state-of-the-art of metal-assisted mechanical exfoliation of large-area TMDs membranes. Current understanding of the interaction between metal and TMDs, with a special focus on the MoS_2/Au model system has been presented, considering different models accounting for the monolayer-selective exfoliation on Au and other metal surfaces. The key experimental parameters to be controlled in order to maximize the monolayer exfoliation yield, i.e., the Au surface roughness and surface contaminations arising from exposure to air, have been discussed. Furthermore, the main experimental implementations for Au-assisted exfoliation and transfer of large-area 1L MoS_2 to arbitrary substrates have been illustrated, comparing advantages and drawbacks. State-of-the-art device demonstrators realized using as-exfoliated 1L MoS_2 membranes on Au (e.g., Au/MoS_2/Au memristors) or transferred membranes on insulating substrates (e.g., large-area photodetectors and back-gated FET arrays) are presented. Furthermore, recently demonstrated enhanced atomic layer deposition of high-κ dielectrics on Au-supported 1L MoS_2, and its potential advantages in top-gated FET fabrication was discussed. Perspectives of sequential metal-assisted exfoliation and transfer of 2D materials in the realization of arrays of 2D heterojunction devices (including Moirè superlattice devices) are envisaged. Finally, we discussed open challenges for widespread application of this method, including the need of improved synthetic approaches for large-area bulk crystals of

© 2024 The Author(s). Advanced Functional Materials published by Wiley-VCH GmbH

16163028, 0, Downloaded from https://onlinelibrary.wiley.com/doi/10.1002/adfm.202414532 by CNR Bologna, Wiley Online Library on [25/11/2024]. See the Terms and Conditions (https://onlinelibrary.wiley.com/terms-and-conditions) on Wiley Online Library for rules of use; OA articles are governed by the applicable Creative Commons License

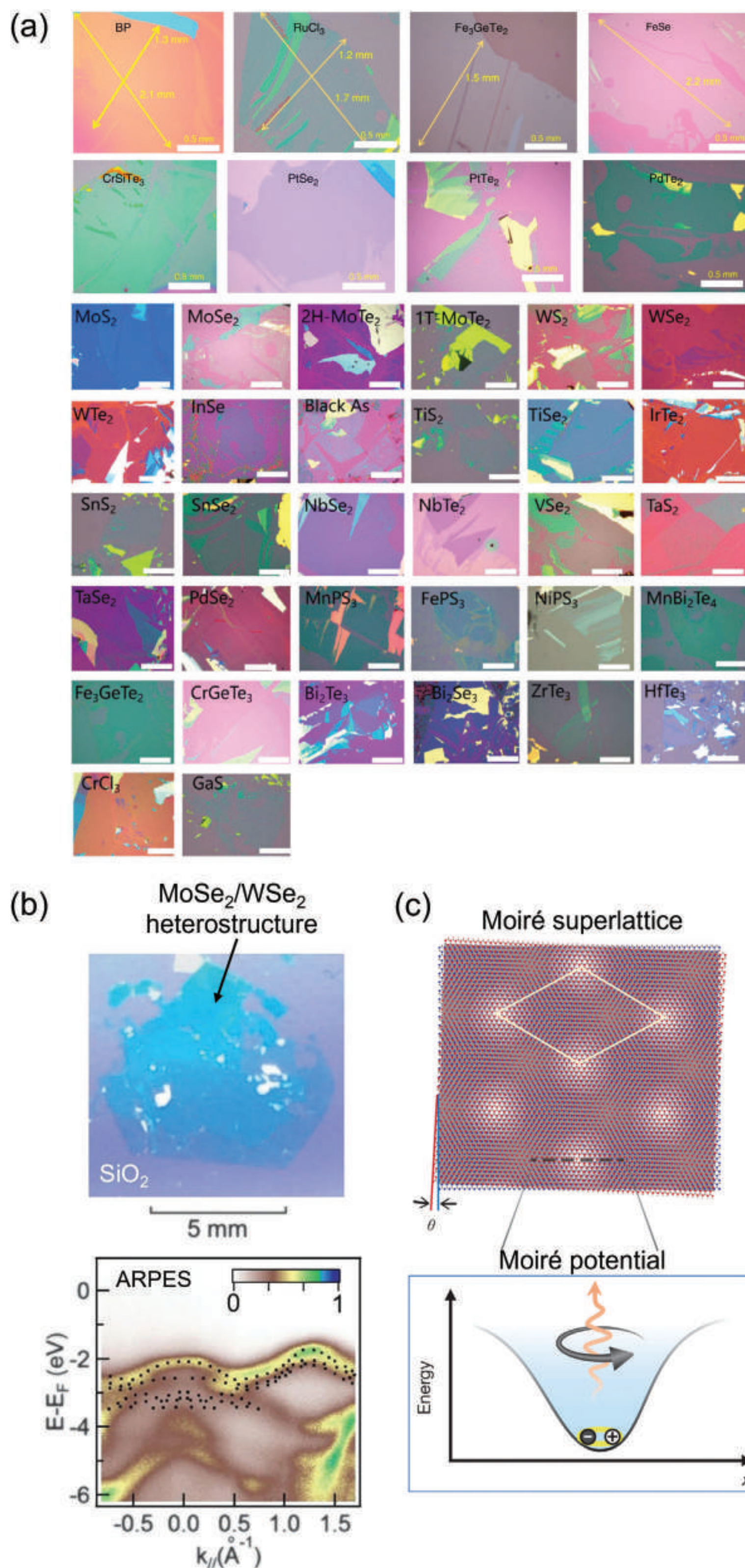

Figure 15. a) Optical images of large-area membranes of 2D materials exfoliated on the surface of Au films. b) Optical image and energy bandstructure (by ARPES) of a cm^2 $MoSe_2/WSe_2$ heterostructure on an SiO_2/Si substrate, fabricated by sequential Au-assisted exfoliation and transfer of the two membranes. c) Schematic of a Moiré superlattice and the corresponding Moiré potential for TMDs-based heterostructures. (a) Adapted with permission.[99] Copyright 2020, Springer Nature. (b) Adapted with permission.[88] Copyright 2020, AAAS. (c) Adapted with permission.[157] Copyright 2019, Springer Nature.

© 2024 The Author(s). Advanced Functional Materials published by Wiley-VCH GmbH

16163028, 0, Downloaded from https://onlinelibrary.wiley.com/doi/10.1002/adfm.202414532 by CNR Bologna, Wiley Online Library on [25/11/2024]. See the Terms and Conditions (https://onlinelibrary.wiley.com/terms-and-conditions) on Wiley Online Library for rules of use; OA articles are governed by the applicable Creative Commons License

different 2D materials, and the standardization of metal surfaces preparation and transfer methods.

Acknowledgements

This work was supported, in part, by European Union (NextGeneration EU), through the MUR-PNRR project SAMOTHRACE (ECS00000022) and the PRIN2022 project "2DIntegratE" (2022RHRZN2).

Open access publishing facilitated by Consiglio Nazionale delle Ricerche, as part of the Wiley - CRUI-CARE agreement.

Conflict of Interest

The authors declare no conflict of interest.

Author Contributions

Conceptualization, S.E.P. and F.G.; writing—original draft preparation, S.E.P. and F.G.; writing—review and editing, S.E.P., E.S., F.R., and F.G.; supervision, F.G.; funding acquisition, F.R. and F.G.

Keywords

devices, exfoliation, gold, transfer, transition metal dichalcogenides

Received: August 9, 2024
Revised: October 24, 2024
Published online:

[1] K. S. Novoselov, A. K. Geim, S. V. Morozov, D. E. Jiang, Y. Zhang, S. V. Dubonos, I. V. Grigorieva, A. A. Firsov, *Science* **2004**, *306*, 666.
[2] A. K. Geim, I. V. Grigorieva, *Nature* **2013**, *499*, 419.
[3] J. Zhou, L. Shen, M. D. Costa, K. A. Persson, S. P. Ong, P. Huck, Y. Lu, X. Ma, Y. Chen, H. Tang, Y. P. Feng, *Sci. Data* **2019**, *6*, 86.
[4] A. Molle, J. Goldberger, M. Houssa, Y. Xu, S. C. Zhang, D. Akinwande, *Nat. Mater.* **2017**, *16*, 163.
[5] Z. Y. Al Balushi, K. Wang, R. K. Ghosh, R. A. Vilá, S. M. Eichfeld, J. D. Caldwell, X. Qin, Y. C. Lin, P. A. DeSario, G. Stone, S. Subramanian, D. F. Paul, R. M. Wallace, S. Datta, J. M. Redwing, J. A. Robinson, *Nat. Mater.* **2016**, *15*, 1166.
[6] G. Sfuncia, G. Nicotra, F. Giannazzo, B. Pécz, G. K. Gueorguiev, A. Kakanakova-Georgieva, *CrystEngComm* **2023**, *25*, 5810.
[7] B. Pécz, G. Nicotra, F. Giannazzo, R. Yakimova, A. Koos, A. Kakanakova-Georgieva, *Adv. Mater.* **2021**, *33*, 202006660.
[8] A. Kakanakova-Georgieva, G. K. Gueorguiev, D. G. Sangiovanni, N. Suwannaharn, I. G. Ivanov, I. Cora, B. Pécz, G. Nicotra, F. Giannazzo, *Nanoscale* **2020**, *12*, 19470.
[9] A. Kakanakova-Georgieva, F. Giannazzo, G. Nicotra, I. Cora, G. K. Gueorguiev, P. Persson, B. Pécz, *Appl. Surf. Sci.* **2021**, *548*, 149275.
[10] F. Turker, C. Dong, M. T. Wetherington, H. El-Sherif, S. Holoviak, Z. J. Trdinich, E. T. Lawson, G. Krishnan, C. Whittier, S. B. Sinnott, N. Bassim, J. A. Robinson, *Adv. Funct. Mater.* **2023**, *33*, 2210404.
[11] K. F. Mak, C. Lee, J. Hone, J. Shan, T. F. Heinz, *Phys. Rev. Lett.* **2010**, *105*, 136805.
[12] A. Splendiani, L. Sun, Y. Zhang, T. Li, J. Kim, C. Y. Chim, G. Galli, F. Wang, *Nano Lett.* **2010**, *10*, 1271.
[13] Q. H. Wang, K. Kalantar-Zadeh, A. Kis, J. N. Coleman, M. S. Strano, *Nat. Nanotechnol.* **2012**, *7*, 699.
[14] D. Jariwala, V. K. Sangwan, L. J. Lauhon, T. J. Marks, M. C. Hersam, *ACS Nano* **2014**, *8*, 1102.
[15] T. Nawz, A. Safdar, M. Hussain, D. Sung Lee, M. Siyar, *Crystals* **2020**, *10*, 902.
[16] M. Yi, Z. Shen, *J. Mater. Chem. A* **2015**, *3*, 11700.
[17] B. Radisavljevic, A. Radenovic, J. Brivio, V. Giacometti, A. Kis, *Nat. Nanotechnol.* **2011**, *6*, 147.
[18] B. Radisavljevic, M. B. Whitwick, A. Kis, *ACS Nano* **2011**, *5*, 9934.
[19] O. Lopez-Sanchez, D. Lembke, M. Kayci, A. Radenovic, A. Kis, *Nat. Nanotechnol.* **2013**, *8*, 497.
[20] H. Li, Z. Yin, Q. He, H. Li, X. Huang, G. Lu, D. W. H. Fam, A. l. Y. Tok, Q. Zhang, H. Zhang, *Small* **2012**, *8*, 63.
[21] Z. Yin, H. Li, H. o. Li, L. Jiang, Y. Shi, Y. Sun, G. Lu, Q. Zhang, X. Chen, H. Zhang, *ACS Nano* **2012**, *6*, 74.
[22] H. S. Lee, S. W. Min, Y. G. Chang, M. K. Park, T. Nam, H. Kim, J. H. Kim, S. Ryu, S. Im, *Nano Lett.* **2012**, *12*, 3695.
[23] M. Bernardi, M. Palummo, J. C. Grossman, *Nano Lett.* **2013**, *13*, 3664.
[24] F. Liu, *Prog. Surf. Sci.* **2021**, *96*, 100626.
[25] M. Heyl, E. J. List-Kratochvil, *Appl. Phys. A* **2023**, *129*, 16.
[26] L. Pirker, J. Honolka, M. Velický, O. Frank, *2D Mater.* **2024**, *11*, 022003.
[27] L. Tang, J. Tan, H. Nong, B. Liu, H. M. Cheng, *Acc. Mater. Res.* **2020**, *2*, 36.
[28] A. Bala, A. Sen, J. Shim, S. Gandla, S. Kim, *ACS Nano* **2023**, *17*, 13784.
[29] T. Kwak, J. Lee, B. So, U. Choi, O. Nam, *J. of Cryst. Growth* **2019**, *510*, 50.
[30] R. Kitaura, *Vac. Surf. Sci.* **2019**, *62*, 605.
[31] J. -G. Song, J. Park, W. Lee, T. Choi, H. Jung, C. W. Lee, S. -H. Hwang, J. M. Myoung, J. -H. Jung, S. -H. Kim, C. Lansalot-Matras, H. Kim, *ACS Nano* **2013**, *7*, 11333.
[32] K. S. Novoselov, A. C. Neto, *Phys. Scr.* **2012**, *T146*, 014006.
[33] Y. Xu, L. Yan, X. Li, H. Xu, *Sci. Rep.* **2019**, *9*, 2931.
[34] M. Heyl, D. Burmeister, T. Schultz, S. Pallasch, G. Ligorio, N. Koch, E. J. List-Kratochvil, *Phys. Status Solidi RRL* **2020**, *14*, 2000408.
[35] Y. H. Lee, X. Q. Zhang, W. Zhang, M. T. Chang, C. T. Lin, K. D. Chang, Y. C. Yu, J. T. W. Wang, C. S. Chang, L. J. Li, T. W. Lin, *Adv. Mater.* **2012**, *24*, 2320.
[36] Y. Cao, X. Luo, S. Han, C. Yuan, Y. Yang, Q. Li, T. Yu, S. Ye, *Chem. Phys. Lett.* **2015**, *631*, 30.
[37] P. Kumar, B. Viswanath, *Cryst. Growth Des.* **2016**, *16*, 7145.
[38] H. Yu, M. Liao, W. Zhao, G. Liu, X. J. Zhou, Z. Wei, X. Xu, K. Liu, Z. Hu, K. Deng, S. Zhou, J. A. Shi, L. Gu, C. Shen, T. Zhang, L. Du, L. Xie, J. Zhu, W. Chen, R. Yang, D. Shi, G. Zhang, *ACS Nano* **2017**, *11*, 12001.
[39] D. Dumcenco, D. Ovchinnikov, K. Marinov, P. Lazic, M. Gibertini, N. Marzari, O. L. Sanchez, Y. C. Kung, D. Krasnozhon, M. W. Chen, S. Bertolazzi, P. Gillet, A. F. i Morral, A. Radenovic, A. Kis, *ACS Nano* **2015**, *9*, 4611.
[40] S. E. Panasci, A. Koos, E. Schilirò, S. Di Franco, G. Greco, P. Fiorenza, F. Roccaforte, S. Agnello, M. Cannas, F. M. Gelardi, A. Sulyok, M. Nemeth, B. Pécz, F. Giannazzo, *Nanomaterials* **2022**, *12*, 182.
[41] S. E. Panasci, E. Schilirò, A. Koos, F. Roccaforte, M. Cannas, S. Agnello, B. Pécz, F. Giannazzo, *Appl. Phys. Lett.* **2024**, *124*, 243101.
[42] M. Španková, M. Sojková, E. Dobročka, P. Hutár, M. Bodík, F. Munnik, M. Hulman, Š. Chromik, *Appl. Surf. Sci.* **2021**, *540*, 148240.
[43] R. I. Romanov, M. G. Kozodaev, D. I. Myakota, A. G. Chernikova, S. M. Novikov, V. S. Volkov, A. S. Slavich, S. S. Zarubin, P. S. Chizhov, R. R. Khakimov, A. A. Chouprik, C. S. Hwang, A. M. Markeev, *ACS Appl. Nano Mater.* **2019**, *2*, 7521.
[44] S. Vangelista, E. Cinquanta, C. Martella, M. Alia, M. Longo, A. Lamperti, R. Mantovan, F. B. Basset, F. Pezzoli, A. Molle, *Nanotechnology* **2016**, *27*, 175703.

© 2024 The Author(s). Advanced Functional Materials published by Wiley-VCH GmbH

16163028, 0, Downloaded from https://onlinelibrary.wiley.com/doi/10.1002/adfm.202414532 by CNR Bologna, Wiley Online Library on [25/11/2024]. See the Terms and Conditions (https://onlinelibrary.wiley.com/terms-and-conditions) on Wiley Online Library for rules of use; OA articles are governed by the applicable Creative Commons License

[45] S. Najmaei, Z. Liu, W. Zhou, X. Zou, G. Shi, S. Lei, B. I. Yakobson, J. C. Idrobo, P. M. Ajayan, J. Lou, *Nat. Mater.* **2013**, *12*, 754.
[46] S. Najmaei, J. Yuan, J. Zhang, P. Ajayan, J. Lou, *Acc. Chem. Res.* **2015**, *48*, 31.
[47] F. Giannazzo, S. E. Panasci, E. Schilirò, F. Roccaforte, A. Koos, M. Nemeth, B. Pécz, *Adv. Mater. Interfaces* **2022**, *9*, 2200915.
[48] F. Giannazzo, S. E. Panasci, E. Schilirò, G. Greco, F. Roccaforte, G. Sfuncia, G. Nicotra, M. Cannas, S. Agnello, E. Frayssinet, Y. Cordier, A. Michon, A. Koos, B. Pécz, *Appl. Surf. Sci.* **2023**, *631*, 157513.
[49] F. Esposito, M. Bosi, G. Attolini, F. Rossi, S. E. Panasci, P. Fiorenza, F. Giannazzo, F. Fabbri, L. Seravalli, *Appl. Surf. Sci.* **2023**, *639*, 158230.
[50] C. Ahn, J. Lee, H. U. Kim, H. Bark, M. Jeon, G. H. Ryu, Z. Lee, G. Y. Yeom, K. Kim, J. Jung, Y. Kim, C. Lee, T. Kim, *Adv. Mater.* **2015**, *27*, 5223.
[51] A. Bala, N. Liu, A. Sen, Y. Cho, P. Pujar, B. So, S. Kim, *Adv. Funct. Mater.* **2022**, *32*, 2205106.
[52] K. Kang, S. Xie, L. Huang, Y. Han, P. Y. Huang, K. F. Mak, C. J. Kim, D. Muller, J. Park, *Nature* **2015**, *520*, 656.
[53] D. Jayachandran, R. Pendurthi, M. U. Karim Sadaf, N. U. Sakib, A. Pannone, C. Chen, Y. Han, N. Trainor, S. Kumari, T. V. Mc Knight, J. M. Redwing, Y. Yang, S. Das, *Nature* **2024**, *625*, 276.
[54] J. Zhu, J. H. Park, S. A. Vitale, W. Ge, G. S. Jung, J. Wang, M. Mohamed, T. Zhang, M. Ashok, M. Xue, X. Zheng, Z. Wang, J. Hansryd, A. P. Chandrakasan, J. Kong, T. Palacios, *Nat. Nanotechnol.* **2023**, *18*, 456.
[55] T. Jurca, M. J. Moody, A. Henning, J. D. Emery, B. Wang, J. M. Tan, T. L. Lohr, L. J. Lauhon, T. J. Marks, *Angew. Chem., Int. Ed.* **2017**, *56*, 4991.
[56] D. H. Kim, J. C. Park, J. Park, D.-Y. Cho, W.-H. Kim, B. Shong, J.-H. Ahn, T. J. Park, *Chem. Mater.* **2021**, *33*, 4099.
[57] H. Liu, L. Chen, H. Zhu, Q.-Q. Sun, S.-J. Ding, P. Zhou, D. W. Zhang, *Nano Res.* **2020**, *13*, 1644.
[58] M. I. Serna, S. H. Yoo, S. Moreno, Y. Xi, J. P. Oviedo, H. Choi, H. N. Alshareef, M. J. Kim, M. Minary-Jolandan, M. A. Quevedo-Lopez, *ACS Nano* **2016**, *10*, 6054.
[59] F. Bertoldo, R. R. Unocic, Y. C. Lin, X. Sang, A. A. Puretzky, Y. Yu, D. Miakota, C. M. Rouleau, J. Schou, K. S. Thygesen, D. B. Geohegan, S. Canulescu, *ACS Nano* **2021**, *15*, 2858.
[60] F. Giannazzo, S. E. Panasci, E. Schilirò, P. Fiorenza, G. Greco, F. Roccaforte, M. Cannas, S. Agnello, A. Koos, B. Pécz, M. Španková, S. Chromik, *Adv. Mater. Interfaces* **2023**, *10*, 221502.
[61] L. A. Walsh, R. Addou, R. M. Wallace, C. L. Hinkle, *Molecular Beam Epitaxy of Transition Metal Dichalcogenides*, Elsevier, Amsterdam **2018**, pp. 515.
[62] D. Fu, X. Zhao, Y. Y. Zhang, L. Li, H. Xu, A. R. Jang, S. I. Yoon, P. Song, S. M. Poh, T. Ren, Z. Ding, W. Fu, T. J. Shin, H. S. Shin, S. T. Pantelides, W. Zhou, K. P. Loh, *Amer. Chem. Soc.* **2017**, *139*, 9392.
[63] H. Zeng, B. Zhu, K. Liu, J. Fan, X. Cui, Q. M. Zhang, *Phys. Rev. B* **2012**, *86*, 241301.
[64] P. H. Tan, W. P. Han, W. J. Zhao, Z. H. Wu, K. Chang, H. Wang, Y. F. Wang, N. Bonini, N. Marzari, N. Pugno, G. Savini, A. Lombardo, A. C. Ferrari, *Nat. Mater.* **2012**, *11*, 294.
[65] J. N. Coleman, M. Lotya, A. O'Neill, S. D. Bergin, P. J. King, U. Khan, K. Young, A. Gaucher, S. De, R. J. Smith, I. V. Shvets, S. K. Arora, G. Stanton, H. Y. Kim, K. Lee, G. T. Kim, G. S. Duesberg, T. Hallam, J. J. Boland, J. J. Wang, J. F. Donegan, J. C. Grunlan, G. Moriarty, A. Shmeliov, R. J. Nicholls, J. M. Perkins, E. M. Grieveson, K. Theuwissen, D. W. Mccomb, P. D. Nellist, et al., *Science* **2011**, *331*, 568.
[66] V. Nicolosi, M. Chhowalla, M. G. Kanatzidis, M. S. Strano, J. N. Coleman, *Science* **2013**, *340*, 1226419.
[67] C. Huo, Z. Yan, X. Song, H. Zeng, *Sci. Bull.* **2015**, *60*, 1994.
[68] M. A. Py, R. R. Haering, *Can. J. Phys.* **1983**, *61*, 76.
[69] G. Eda, H. Yamaguchi, D. Voiry, T. Fujita, M. Chen, M. Chhowalla, *Nano Lett.* **2011**, *11*, 5111.
[70] G. L. Frey, K. J. Reynolds, R. H. Friend, H. Cohen, Y. Feldman, *J. Am. Chem. Soc.* **2003**, *125*, 5998.
[71] K. E. Dungey, M. D. Curtis, J. E. Penner-Hahn, *Chem. Mater.* **1998**, *10*, 2152.
[72] D. J. Finn, M. Lotya, G. Cunningham, R. J. Smith, D. McCloskey, J. F. Donegan, J. N. Coleman, *J. Mater. Chem. C* **2014**, *2*, 925.
[73] O. A. Moses, L. Gao, H. Zhao, Z. Wang, M. L. Adam, Z. Sun, K. Liu, J. Wang, Y. Lu, Z. Yin, X. Yu, *Mater. Today* **2021**, *50*, 116.
[74] S. Ji, Z. Yang, C. Zhang, Z. Liu, W. W. Tjiu, I. Y. Phang, Z. Zhang, J. Pan, T. Liu, *Electrochim. Acta* **2013**, *109*, 269.
[75] D. Gopalakrishnan, D. Damien, M. M. Shaijumon, *ACS Nano* **2014**, *8*, 5297.
[76] G. S. Bang, K. W. Nam, J. Y. Kim, J. Shin, J. W. Choi, S. Y. Choi, *ACS Appl. Mater. Interfaces* **2014**, *6*, 7084.
[77] X. L. Li, T. C. Li, S. Huang, J. Zhang, M. E. Pam, H. Y. Yang, *ChemSusChem* **2020**, *13*, 1379.
[78] R. Kumar, S. Sahoo, E. Joanni, R. K. Singh, R. M. Yadav, R. K. Verma, D. P. Singh, W. K. Tan, A. P. del Pino, S. A. Moshkalev, A. Matsuda, *Nano Res.* **2019**, *12*, 2655.
[79] L. Guan, B. Xing, X. Niu, D. Wang, Y. Yu, S. Zhang, X. Yan, Y. Wang, J. Sha, *Chem. Commun.* **2018**, *54*, 595.
[80] J. Shim, S. H. Bae, W. Kong, D. Lee, K. Qiao, D. Nezich, Y. J. Park, R. Zhao, S. Sundaram, X. Li, H. Yeon, C. Choi, H. Kum, R. Yue, G. Zhou, Y. Ou, K. Lee, J. Moodera, X. Zhao, J. H. Ahn, C. Hinkle, A. Ougazzaden, J. Kim, *Science* **2018**, *362*, 665.
[81] H. M. Gramling, C. M. Towle, S. B. Desai, H. Sun, E. C. Lewis, V. D. Nguyen, J. W. Ager, D. Chrzan, E. M. Yeatman, A. Javey, H. Taylor, *ACS Appl. Mater. Interfaces* **2019**, *1*, 407.
[82] M. Heyl, S. Grützmacher, S. Rühl, G. Ligorio, N. Koch, E. J. W. List-Kratchvil, *Adv. Mater. Interfaces* **2022**, *9*, 2200362.
[83] Z. Li, L. Ren, S. Wang, X. Huang, Q. Li, Z. Lu, S. Ding, H. Deng, P. Chen, J. Lin, Y. Hu, L. Liao, Y. Liu, *ACS Nano* **2021**, *15*, 13839.
[84] S. Ding, C. Liu, Z. Li, Z. Lu, Q. Tao, D. Lu, Y. Chen, W. Tong, L. Liu, W. Li, L. Ma, X. Yang, Z. Xiao, Y. Wang, L. Liao, Y. Liu, *ACS Nano* **2023**, *18*, 1195.
[85] A. Grubišić-Čabo, M. Michiardi, C. E. Sanders, M. Bianchi, D. Curcio, D. Phuyal, M. H. Berntsen, Q. Guo, M. Dendzik, *Adv. Sci.* **2023**, *10*, 2301243.
[86] H. Li, J. Wu, Z. Yin, H. Zhang, *Acc. Chem. Res.* **2014**, *47*, 1067.
[87] S. E. Panasci, E. Schilirò, G. Greco, M. Cannas, F. M. Gelardi, S. Agnello, F. Roccaforte, F. Giannazzo, *ACS Appl. Mater. Interfaces* **2021**, *13*, 31248.
[88] F. Liu, W. Wu, Y. Bai, S. H. Chae, Q. Li, J. Wang, J. Hone, X. Y. Zhu, *Science* **2020**, *367*, 903.
[89] H. Häkkinen, *Nat. Chem.* **2012**, *4*, 443.
[90] D. L. Kokkin, R. Zhang, T. C. Steimle, I. A. Wyse, B. W. Pearlman, T. D. Varberg, *J. Phys. Chem. A* **2015**, *119*, 11659.
[91] R. L. Whetten, R. C. Price, *Science* **2007**, *318*, 407.
[92] E. Pensa, E. Cortés, G. Corthey, P. Carro, C. Vericat, M. H. Fonticelli, G. Benítez, A. A. Rubert, R. C. Salvarezza, *Acc. Chem. Res.* **2012**, *45*, 1183.
[93] H. Zhong, R. Quhe, Y. Wang, Z. Ni, M. Ye, Z. Song, Y. Pan, J. Yang, L. Yang, M. Lei, J. Shi, J. Lu, *Sci. Rep.* **2016**, *6*, 21786.
[94] M. Farmanbar, G. Brocks, *Phys. Rev. B: Condens. Matter Mater. Phys.* **2016**, *93*, 085304.
[95] M. Velický, G. E. Donnelly, W. R. Hendren, S. McFarland, D. Scullion, W. J. DeBenedetti, G. C. Correa, Y. Han, A. J. Wain, M. A. Hines, D. A. Muller, K. S. Novoselov, H. D. Abruña, R. M. Bowman, E. J. G. Santos, F. Huang, *ACS Nano* **2018**, *12*, 10463.
[96] Y. Liu, Y. Huang, X. Duan, *Nature* **2019**, *567*, 323.
[97] A. H. Woomer, D. L. Druffel, J. D. Sundberg, J. T. Pawlik, S. C. Warren, *J. Am. Chem. Soc.* **2019**, *141*, 10300.

© 2024 The Author(s). Advanced Functional Materials published by Wiley-VCH GmbH

16163028, 0, Downloaded from https://onlinelibrary.wiley.com/doi/10.1002/adfm.202414532 by CNR Bologna, Wiley Online Library on [25/11/2024]. See the Terms and Conditions (https://onlinelibrary.wiley.com/terms-and-conditions) on Wiley Online Library for rules of use; OA articles are governed by the applicable Creative Commons License

[98] H. Zhong, R. Quhe, Y. Wang, Z. Ni, M. Ye, Z. Song, Y. Pan, J. Yang, L. Yang, M. Lei, J. Shi, J. Lu, *Sci. Rep.* **2016**, *6*, 21786.
[99] Y. Huang, Y. H. Pan, R. Yang, L. H. Bao, L. Meng, H. L. Luo, Y. Q. Cai, G. D. Liu, W. J. Zhao, Z. Zhou, L. M. Wu, Z. L. Zhu, M. Huang, L. W. Liu, L. Liu, P. Cheng, K. H. Wu, S. B. Tian, C. Z. Gu, Y. G. Shi, Y. F. Guo, Z. G. Cheng, J. P. Hu, L. Zhao, G. H. Yang, E. Sutter, P. Sutter, Y. L. Wang, W. Ji, X. J. Zhou, et al., *Nat. Commun.* **2020**, *11*, 2453.
[100] J. S. Qiao, X. H. Kong, Z. X. Hu, F. Yang, W. Ji, *Nat. Commun.* **2014**, *5*, 4475.
[101] Z.-X. Hu, X. Kong, J. Qiao, B. Normand, W. Ji, *Nanoscale* **2016**, *8*, 2740.
[102] J. Qiao, Y. Pan, F. Yang, C. Wang, Y. Chai, W. Ji, *Sci. Bull.* **2018**, *63*, 159.
[103] M. Velický, G. E. Donnelly, W. R. Hendren, W. J. I. DeBenedetti, M. A. Hines, K. S. Novoselov, H. D. Abruña, F. Huang, O. Frank, *Adv. Mater. Interfaces* **2020**, *7*, 2001324.
[104] H. Sun, E. W. Sirott, J. Mastandrea, H. M. Gramling, Y. Zhou, M. Poschmann, H. K. Taylor, J. W. Ager, D. C. Chrzan, *Phys. Rev. Mater.* **2018**, *2*, 094004.
[105] A. C. Johnston, S. I. Khondaker, *Adv. Mater. Interfaces* **2022**, *9*, 2200106.
[106] A. Corletto, M. Fronzi, A. K. Joannidis, P. C. Sherrell, M. J. Ford, D. A. Winkler, J. G. Shapter, J. Bullock, A. V. Ellis, *Adv. Mater. Interfaces* **2024**, *11*, 2300686.
[107] X. Zhang, X. F. Qiao, W. Shi, J. B. Wu, D. S. Jiang, P. H. Tan, *Chem. Soc. Rev.* **2015**, *44*, 2757.
[108] A. Molina-Sanchez, L. Wirtz, *Phys. Rev. B* **2011**, *84*, 155413.
[109] N. Ferralis, *J. Mater. Sci.* **2010**, *45*, 5135.
[110] R. Saito, Y. Tatsumi, S. Huang, X. Ling, M. S. Dresselhaus, *J. Phys. Condens. Matter* **2016**, *28*, 353002.
[111] M. Velický, A. Rodriguez, M. Bousa, A. V. Krayev, M. Vondracek, J. Honolka, M. Ahmadi, G. E. Donnelly, F. Huang, H. D. Abruña, K. S. Novoselov, O. Frank, *J. Phys. Chem. Lett.* **2020**, *11*, 6112.
[112] E. Pollmann, S. Sleziona, T. Foller, U. Hagemann, C. Gorynski, O. Petri, L. Madauß, L. Breuer, M. Schleberger, *ACS Omega* **2021**, *6*, 15929.
[113] J. Pető, G. Dobrik, G. Kukucska, P. Vancsó, A. A. Koós, J. Koltai, P. Nemes-Incze, C. Hwang, L. Tapasztó, *npj 2D Mater. Appl.* **2019**, *3*, 39.
[114] S. Yasuda, R. Takahashi, R. Osaka, R. Kumagai, Y. Miyata, S. Okada, Y. Hayamizu, K. Murakoshi, *Small* **2017**, *13*, 1700748.
[115] B. Zou, Z. Wu, Y. Zhou, Y. Zhou, J. Wang, L. Zhang, F. Cao, H. Sun, *Phys. Status Solidi RRL* **2021**, *15*, 2100385.
[116] X. Huang, L. Zhang, L. Liu, Y. Qin, Q. Fu, Q. Wu, R. Yang, J. P. LV, Z. Ni, L. Liu, W. Ji, Y. Wang, X. Zhou, Y. Huang, *Sci. China Inf. Sci.* **2021**, *64*, 140406.
[117] S. M. Hus, R. Ge, P. A. Chen, L. Liang, G. E. Donnelly, W. Ko, F. Huang, M. H. Chiang, A. P. Li, D. Akinwande, *Nat. Nanotechnol.* **2021**, *16*, 58.
[118] E. Schilirò, S. E. Panasci, A. M. Mio, G. Nicotra, S. Agnello, B. Pecz, G. Z. Radnoczi, I. Deretzis, A. La Magna, F. Roccaforte, R. Lo Nigro, F. Giannazzo, *Appl. Surf. Sci.* **2023**, *630*, 157476.
[119] S. E. Panasci, E. Schilirò, F. Migliore, M. Cannas, F. M. Gelardi, F. Roccaforte, F. Giannazzo, S. Agnello, *Appl. Phys. Lett.* **2021**, *119*, 093103.
[120] A. Michail, N. Delikoukos, J. Parthenios, C. Galiotis, K. Papagelis, *Appl. Phys. Lett.* **2016**, *108*, 173102.
[121] W. H. Chae, J. D. Cain, E. D. Hanson, A. A. Murthy, V. P. Dravid, *Appl. Phys. Lett.* **2017**, *111*, 143106.
[122] D. Lloyd, X. Liu, J. W. Christopher, L. Cantley, A. Wadehra, B. L. Kim, B. B. Goldberg, A. K. Swan, J. S. Bunch, *Nano Lett.* **2016**, *16*, 5836.
[123] B. Chakraborty, A. Bera, D. Muthu, S. Bhowmick, U. V. Waghmare, A. Sood, *Phys. Rev. B: Condens. Matter Mater. Phys.* **2012**, *85*, 161403.
[124] G. Z. Magda, J. Pető, G. Dobrik, C. Hwang, L. P. Biró, L. Tapasztó, *Sci. Rep.* **2015**, *5*, 14714.
[125] S. Sarkar, P. Kratzer, *J. Phys. Chem. C* **2021**, *125*, 26645.
[126] U. Bhanu, M. R. Islam, L. Tetard, S. I. Khondaker, *Sci. Rep.* **2014**, *4*, 5575.
[127] Y. Liu, J. Guo, E. Zhu, L. Liao, S. J. Lee, M. Ding, I. Shakir, V. Gambin, Y. Huang, X. Duan, *Nature* **2018**, *557*, 696.
[128] S. B. Desai, S. R. Madhvapathy, M. Amani, D. Kiriya, M. Hettick, M. Tosun, Y. Zhou, M. Dubey, J. W. Ager, D. Chrzan, A. Javey, *Adv. Mater.* **2016**, *28*, 4053.
[129] P. Brus, V. Zatko, M. Galbiati, F. Godel, S. Collin, B. Servet, S. Xavier, R. Aubry, P. Garabedian, M. B. Martin, B. Dlubak, P. Seneor, O. Bezencenet, *Adv. Electron. Mater.* **2021**, *7*, 2001109.
[130] C. Kim, K. Y. Lee, I. Moon, S. Issarapanacheewin, W. J. Yoo, *Nanoscale* **2019**, *11*, 18246.
[131] W. Zheng, B. Yuan, M. A. Villena, K. Zhu, S. Pazos, Y. Shen, Y. Yuan, Y. Ping, C. Liu, X. Zhang, X. Zhang, M. Lanza, *Mater. Sci. Eng. R* **2024**, *160*, 100831.
[132] Z. Cheng, Q. Zhou, C. Wang, Q. Li, C. Wang, Y. Fang, *Nano Lett.* **2011**, *11*, 767.
[133] A. Pirkle, J. Chan, A. Venugopal, D. Hinojos, C. W. Magnuson, S. McDonnell, L. Colombo, E. M. Vogel, R. S. Ruoff, R. M. Wallace, *Appl. Phys. Lett.* **2011**, *99*, 122108.
[134] S. Sahu, G. Haider, A. Rodriguez, J. Plšek, M. Mergl, M. Kalbáč, O. Frank, M. Velický, *Adv. Mater. Technol.* **2023**, *8*, 2201993.
[135] E. Schilirò, R. Lo Nigro, S. E. Panasci, S. Agnello, M. Cannas, F. M. Gelardi, F. Roccaforte, F. Giannazzo, *Adv. Mater. Interfaces* **2021**, *8*, 2101117.
[136] L. Chua, *IEEE Trans. Circuit Theory* **1971**, *18*, 507.
[137] D. J. Wouters, R. Waser, M. Wuttig, *Proc. IEEE* **2015**, *103*, 1274.
[138] R. Ge, X. Wu, M. Kim, J. Shi, S. Sonde, L. Tao, Y. Zhang, J. C. Lee, D. Akinwande, *Nano Lett.* **2018**, *18*, 434.
[139] M. Wang, S. Cai, C. Pan, C. Wang, X. Lian, Y. Zhuo, K. Xu, T. Cao, X. Pan, B. Wang, S. J. Liang, J. J. Yang, P. Wang, F. Miao, *Nat. Electron.* **2018**, *1*, 130.
[140] R. Xu, H. Jang, M. H. Lee, D. Amanov, Y. Cho, H. Kim, S. Park, H. J. Shin, D. Ham, *Nano Lett.* **2019**, *19*, 2411.
[141] D. Jena, A. Konar, *Phys. Rev. Lett.* **2007**, *98*, 136805.
[142] F. Chen, J. Xia, D. K. Ferry, N. Tao, *Nano Lett.* **2009**, *9*, 2571.
[143] E. Schilirò, R. Lo Nigro, F. Roccaforte, F. Giannazzo, *Appl. Sci.* **2021**, *11*, 11052.
[144] V. A. Fonoberov, A. A. Balandin, *Nano Lett.* **2006**, *6*, 2442.
[145] C. Wirtz, T. Hallam, C. P. Cullen, N. C. Berner, M. O'Brien, M. Marcia, A. Hirsch, G. S. Duesberg, *Chem. Commun.* **2015**, *51*, 16553.
[146] W. C. Shin, T. Y. Kim, O. Sul, B. J. Cho, *Appl. Phys. Lett.* **2012**, *101*, 033507.
[147] J. Kitzmann, A. Göritz, M. Fraschke, M. Lukosius, C. Wenger, A. Wolff, G. Lupina, *Sci. Rep.* **2016**, *6*, 29223.
[148] X. Wang, S. M. Tabakman, H. Dai, *J. Am. Chem. Soc.* **2008**, *130*, 8152.
[149] S. Kim, J. Nah, I. Jo, D. Shahrjerdi, L. Colombo, Z. Yao, E. Tutuc, S. K. Banerjee, *Appl. Phys. Lett.* **2009**, *94*, 062107.
[150] B. Fallahazad, K. Lee, G. Lian, S. Kim, C. Corbet, D. Ferrer, L. Colombo, E. Tutuc, *Appl. Phys. Lett.* **2012**, *100*, 093112.
[151] W. J. Woo, I. K. Oh, B. E. Park, Y. Kim, J. Park, S. Seo, J.-G. Song, H. Jung, D. Kim, J. H. Lim, S. Lee, H. Kim, *2D Mater.* **2019**, *6*, 015019.
[152] L. Cheng, X. Qin, A. T. Lucero, A. Azcatl, J. Huang, R. M. Wallace, K. Cho, J. Kim, *ACS Appl. Mater. Interfaces* **2014**, *6*, 11834.
[153] B. Dlubak, P. R. Kidambi, R. S. Weatherup, S. Hofmann, J. Robertson, *Appl. Phys. Lett.* **2012**, *100*, 173113.
[154] E. Schilirò, R. Lo Nigro, F. Roccaforte, I. Deretzis, A. La Magna, A. Armano, S. Agnello, B. Pécz, I. G. Ivano, R. Yakimova, F. Giannazzo, *Adv. Mater. Interfaces* **2019**, *6*, 1900097.
[155] E. Schilirò, R. Lo Nigro, S. E. Panasci, F. M. Gelardi, S. Agnello, R. Yakimova, F. Roccaforte, F. Giannazzo, *Carbon* **2020**, *169*, 172.

© 2024 The Author(s). Advanced Functional Materials published by Wiley-VCH GmbH

16163028, 0, Downloaded from https://onlinelibrary.wiley.com/doi/10.1002/adfm.202414532 by CNR Bologna, Wiley Online Library on [25/11/2024]. See the Terms and Conditions (https://onlinelibrary.wiley.com/terms-and-conditions) on Wiley Online Library for rules of use; OA articles are governed by the applicable Creative Commons License

[156] W. Li, J. Zhou, S. Cai, Z. Yu, J. Zhang, N. Fang, T. Li, Y. Wu, T. Chen, X. Xie, H. Ma, K. Yan, N. Dai, X. Wu, H. Zhao, Z. Wang, D. He, L. Pan, Y. Shi, P. Wang, W. Chen, K. Nagashio, X. Duan, X. Wang, *Nat. Electron.* **2019**, *2*, 563.
[157] K. L. Seyler, P. Rivera, H. Yu, N. P. Wilson, E. L. Ray, D. G. Mandrus, J. Yan, W. Yao, X. Xu, *Nature* **2019**, *567*, 66.
[158] C. H. Lee, G. H. Lee, A. M. Van Der Zande, W. Chen, Y. Li, M. Han, X. Cui, G. Arefe, C. Nuckolls, T. F. Heinz, J. Hone, P. Kim, *Nat. Nanotechnol.* **2014**, *9*, 676.
[159] R. Cheng, D. Li, H. Zhou, C. Wang, A. Yin, S. Jiang, Y. Liu, Y. Chen, Y. Huang, X. Duan, *Nano Lett.* **2014**, *14*, 5590.
[160] F. Withers, O. Del Pozo-Zamudio, A. Mishchenko, A. Rooney, A. Gholinia, K. Watanabe, T. Taniguchi, S. Haigh, A. Geim, A. Tartakovskii, K. S. Novoselov, *Nat. Mater.* **2015**, *14*, 301.
[161] F. He, Y. Zhou, Z. Ye, S. H. Cho, J. Jeong, X. Meng, Y. Wang, *ACS Nano* **2021**, *15*, 5944.
[162] Y. Cao, V. Fatemi, S. Fang, K. Watanabe, T. Taniguchi, E. Kaxiras, P. Jarillo-Herrero, *Nature* **2018**, *556*, 43.
[163] G. Ni, H. Wang, B.-Y. Jiang, L. Chen, Y. Du, Z. Sun, M. Goldflam, A. Frenzel, X. Xie, M. Fogler, *Nat. Commun.* **2019**, *10*, 4360.
[164] G. Hu, A. Krasnok, Y. Mazor, C.-W. Qiu, A. Alù, *Nano Lett.* **2020**, *20*, 3217.
[165] X. Zhang, F. Lou, C. Li, X. Zhang, N. Jia, T. Yu, J. He, B. Zhang, H. Xia, S. Wang, X. Tao, *CrystEngComm* **2015**, *17*, 4026.
[166] K. K. Tiong, P. C. Liao, C. H. Ho, Y. S. Huang, *J. Cryst. Growth* **1999**, *205*, 543.
[167] G. Fisichella, S. Di Franco, F. Roccaforte, S. Ravesi, F. Giannazzo, *Appl. Phys. Lett.* **2014**, *104*, 233105.

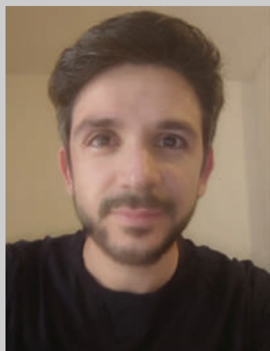

Salvatore Ethan Panasci received M.Sc. degree in Materials Science in 2019 from the University of Padova (Italy) and Ph.D. in Material Science and Nanotechnology in 2022 from the University of Catania (Italy). From 2023 he is temporary researcher at the Institute for Microelectronics and Microsystems of the Italian National Research Council (CNR-IMM) of Catania. Scientific activities: 2D materials (graphene, transition metal dichalcogenides), atomic force microscopy, and Raman/PL spectroscopy.

Emanuela Schilirò received M.Sc. degree in Chemistry of Materials in 2013, and Ph.D. in Material Science and Nanotechnology in 2016, both from the University of Catania. Currently she is temporary researcher at the Institute for Microelectronics and Microsystems of the Italian National Research Council (CNR-IMM) of Catania. Scientific activities: atomic layer deposition (ALD) of high-κ dielectrics on wide bandgap (WBG) semiconductors (SiC, GaN) and on 2D materials.

Fabrizio Roccaforte received M.Sc. degree in Physics from the University of Catania (Italy) in 1996, and Ph.D. from the University of Göttingen (Germany) in 1999. After being visiting scientist at the University of Göttingen, and scientific consultant at STMicroelectronics (Italy), he joined CNR-IMM in Catania as a Researcher in 2001, and he became Senior Researcher in 2007 and Research Director in 2020. His research interests are mainly focused on WBG semiconductors, (e.g., SiC, GaN, Ga_2O_3) materials and devices processing for power electronics devices.

© 2024 The Author(s). Advanced Functional Materials published by Wiley-VCH GmbH

16163028, 0, Downloaded from https://onlinelibrary.wiley.com/doi/10.1002/adfm.202414532 by CNR Bologna, Wiley Online Library on [25/11/2024]. See the Terms and Conditions (https://onlinelibrary.wiley.com/terms-and-conditions) on Wiley Online Library for rules of use; OA articles are governed by the applicable Creative Commons License

Filippo Giannazzo received M.Sc. in Physics (1998) and Ph.D. in Materials Science (2002) from the University of Catania (Italy). He joined CNR-IMM in Catania as a Researcher in 2006 and is Research Director from 2020. His scientific interests include: (i) electrical scanning probe microscopy for the study of charge transport in advanced materials for micro- and nano-electronics; (ii) 2D materials (graphene, TMDs) and their heterostructures with WBG semiconductors (SiC, GaN) for high-frequency and energy efficient electronics.

© 2024 The Author(s). Advanced Functional Materials published by Wiley-VCH GmbH

16163028, 0, Downloaded from https://onlinelibrary.wiley.com/doi/10.1002/adfm.202414532 by CNR Bologna, Wiley Online Library on [25/11/2024]. See the Terms and Conditions (https://onlinelibrary.wiley.com/terms-and-conditions) on Wiley Online Library for rules of use; OA articles are governed by the applicable Creative Commons License